J. Fluid Mech. (2013), *vol.* 731, *pp.* 364–393. © Cambridge University Press 2013
doi:10.1017/jfm.2013.318

Low-dimensional models for compressible temporally developing shear layers

Bashar R. Qawasmeh and Mingjun Wei†

Department of Mechanical and Aerospace Engineering, New Mexico State University, Las Cruces, NM 88003, USA

(Received 1 October 2012; revised 31 May 2013; accepted 17 June 2013; first published online 15 August 2013)

A methodology to achieve extremely-low-dimensional models for temporally developing shear layers is extended from incompressible flows to weakly compressible flows. The key idea is to first remove the slow variation (i.e. viscous growth of shear layers) through symmetry reduction, so that the model reduction using proper orthogonal decomposition (POD)-Galerkin projection in the symmetry-reduced space becomes more efficient. However, for the approach to work for compressible flows, thermodynamic variables need to be retained. We choose the isentropic Navier–Stokes equations for the simplicity and the availability of a well-defined inner product for total energy. To capture basic dynamics, the compressible low-dimensional model requires only two POD modes for each frequency. Thus, a two-mode model is capable of representing single-frequency dynamics such as vortex roll-up, and a four-mode model is capable of representing the nonlinear dynamics involving a fundamental frequency and its subharmonic, such as vortex pairing and merging. The compressible model shows similar behaviour and accuracy as the incompressible model. However, because of the consistency of the inner product defined for POD and for projection in the current compressible model, the orthogonality is kept and it results in simple formulation. More importantly, the inclusion of compressibility opens an entirely new avenue for the discussion of compressibility effect and possible description of aeroacoustics and thermodynamics. Finally, the model is extended to different flow parameters without additional numerical simulation. The extension of the compressible four-mode model includes different Mach numbers and Reynolds numbers. We can clearly observe the change in the nonlinear interaction of modes at two frequencies and the associated promotion or delay of vortex pairing by varying compressibility and viscosity. The dynamic response of the low-dimensional model to different flow parameters is consistent with the vortex dynamics observed in experiments and numerical simulation.

Key words: free shear layers, compressible flows, low-dimensional models

1. Introduction

Free shear layers have historically been benchmark cases before further study of more complex fluid flows (Bradshaw 1977; Saffman & Baker 1979; Ho & Huerre 1984; Chomaz 2005). Lock (1951) derived Blasius-type self-similar solution for a free shear layer between two different parallel streams, and Potter (1957) studied

† Email address for correspondence: mjwei@nmsu.edu

https://doi.org/10.1017/jfm.2013.318 Published online by Cambridge University Press

the interface between two parallel streams and derived an approximate solution at the sixth order. Brown & Roshko (1974) and Winant & Browand (1974) studied experimentally plane turbulent mixing layers formed in the downstream of a splitter plate. The experiments showed clearly the large coherent vortex structures in mixing layers. Winant and Browand described vortex pairing as a process of large vortices forming downstream with the growth of shear layer thickness. Brown and Roshko defined the vortex merging process as a new generation of large vortices being generated from a former generation of smaller vortices. Saffman & Baker (1979) and Aref (1983) focused their studies on vortex motions and depicted the evolution of shear layers as different formations and arrangements of vortices. Free shear layers are often categorized into temporally developing (TD) shear layers and spatially developing (SD) shear layers (Ho & Huerre 1984). Although there is similarity in many aspects of these two categories, Aref & Siggia (1980) pointed out that it is not possible to switch from one to the other by a Galilean transformation. Detailed numerical study of three-dimensional incompressible TD shear layers (Rogers & Moser 1992; Moser & Rogers 1993) showed strong nonlinearity in the shear layer and its role in the transition to turbulence. Compressible shear layers have also been studied extensively in the literature (Bradshaw 1977; Elliott, Samimy & Arnette 1995; Urban & Mungal 2001; Thurow, Samimy & Lempert 2003). Elliott *et al.* (1995) showed that large-scale structures appearing at low Mach number are similar to those observed in incompressible flows. Urban & Mungal (2001) experimentally studied the compressible mixing layer over a range of convective Mach numbers (0.25–0.76) and found that flows at low compressibility have roller-braid structures and flows at high compressibility have instead more diffused and random structures.

Model reduction of shear layers and other more complex flow systems helps in both physical understanding and dynamical control. Proper orthogonal decomposition (POD)-Galerkin projection, as a classic approach, has been successful in many cases (Noack & Eckelmann 1994; Holmes, Lumley & Berkooz 1996; Noack *et al.* 2003; Rowley, Colonius & Murray 2004). Recently, Wei & Rowley (2009) used a modified POD-Galerkin approach to model an incompressible TD shear layer by only two modes for each characteristic frequency. The key idea was to factor out the thickness growth first and then apply POD-Galerkin projection more efficiently in the new symmetry-reduced space, which is related to the technique used for travelling solutions by Rowley & Marsden (2000), and self-similar solutions by Rowley *et al.* (2003). It is emphasized that the thickness growth is not assumed or precomputed in these works. Instead, there is a separate dynamic equation to control the growth rate and is computed simultaneously with other equations from Galerkin projection. A similar idea has then been applied on incompressible SD shear layers by Wei *et al.* (2012). In the current work, we extend the idea to compressible flows for the first time. The major step in the extension to compressible flows is to include the thermodynamic variables and equation. With the assumption of weak compressibility, we choose the isentropic Navier–Stokes equations (Batchelor 2000) for its simplicity. This choice also allows a rigourously defined inner product to represent total energy including both kinetic energy and thermal energy, which therefore defines POD modes and Galerkin projection in a consistent manner for compressible flows (Rowley *et al.* 2004). It is worthwhile to mention that the concept of including the mean flow variation to improve model efficiency has also been used in the method of shift modes proposed by Noack *et al.* (2003), which has recently been extended to a more general scenario (Tadmor *et al.* 2010).

https://doi.org/10.1017/jfm.2013.318 Published online by Cambridge University Press

We then take the study further by applying the model to flow parameters (e.g. Mach number and Reynolds number) different from those used in original numerical simulation. It is emphasized that such an extension of models requires no additional numerical simulation. The extension of models to new Mach numbers and Reynolds numbers is a challenge to the model robustness and even model reduction methodology. Essentially, to adapt the model for new parameters is a key step leading the methodology to a practical level (Deane *et al.* 1991; Lieu & Lesoinne 2004; Schmidt & Glauser 2004; Lieu & Farhat 2007; Amsallem & Farhat 2008).

The rest of the paper is arranged in the following manner. The governing equations are given in § 2, and numerical simulation details are given in § 3. Then, we present the scaling technique and low-dimensional modelling in § 4. In § 5, we compare the low-order models with the analytical solution and numerical simulation, and further extend the model to 'off-design' Mach numbers and Reynolds numbers. The final conclusions are in § 6.

2. Governing equations for modelling

The flow considered here is described by non-dimensional isentropic Navier–Stokes equations, which assume cold flow and moderate Mach number (Zank & Matthaeus 1991; Rowley *et al.* 2004). Therefore, viscous dissipation and heat conduction can be neglected in the energy equation, and density gradients are small and dominated by pressure. The temperature gradients are also considered small. Constant viscosity is assumed in the momentum equation. The detailed derivation from the complete compressible Navier–Stokes equations to the isentropic Navier–Stokes equations is given in appendix A. The final governing equations in non-dimensional form are

$$\frac{\partial u}{\partial t}+u\frac{\partial u}{\partial x}+v\frac{\partial u}{\partial y}+\frac{2}{\gamma-1}a\frac{\partial a}{\partial x}=\frac{1}{Re}\left(\frac{\partial^2 u}{\partial x^2}+\frac{\partial^2 u}{\partial y^2}\right) \tag{2.1a}$$

$$\frac{\partial v}{\partial t}+u\frac{\partial v}{\partial x}+v\frac{\partial v}{\partial y}+\frac{2}{\gamma-1}a\frac{\partial a}{\partial y}=\frac{1}{Re}\left(\frac{\partial^2 v}{\partial x^2}+\frac{\partial^2 v}{\partial y^2}\right) \tag{2.1b}$$

$$\frac{\partial a}{\partial t}+u\frac{\partial a}{\partial x}+v\frac{\partial a}{\partial y}+\frac{\gamma-1}{2}a\left(\frac{\partial u}{\partial x}+\frac{\partial v}{\partial y}\right)=0, \tag{2.1c}$$

where a, u and v are the speed of sound, the velocity along the streamwise direction x and the velocity along the normal direction y, respectively, γ is the specific heat ratio, Re is the Reynolds number defined by the free-stream sound speed a_∞ and the initial vorticity thickness $\delta_{\omega 0}$ at $t=0$. A well-accepted definition for the vortex thickness of shear layers is used (Monkewitz & Huerre 1982; Colonius, Lele & Moin 1997):

$$\delta_\omega=\frac{U_2-U_1}{|\mathrm{d}u/\mathrm{d}y|_{max}}, \tag{2.2}$$

with U_1 and U_2 being the free-stream velocities at $y=-\infty$ and $y=+\infty$ (figure 1).

3. Numerical simulation

Although modelling is based on the isentropic Navier–Stokes equations, it is critical for the numerical simulation to be based on the compressible Navier–Stokes equations in their full formulation (Rowley *et al.* 2004). The simulation code has been extensively validated and used in our previous work in both SD shear layers (Wei & Freund 2006; Wei *et al.* 2012) and TD shear layers (Wei & Rowley 2009).

https://doi.org/10.1017/jfm.2013.318 Published online by Cambridge University Press

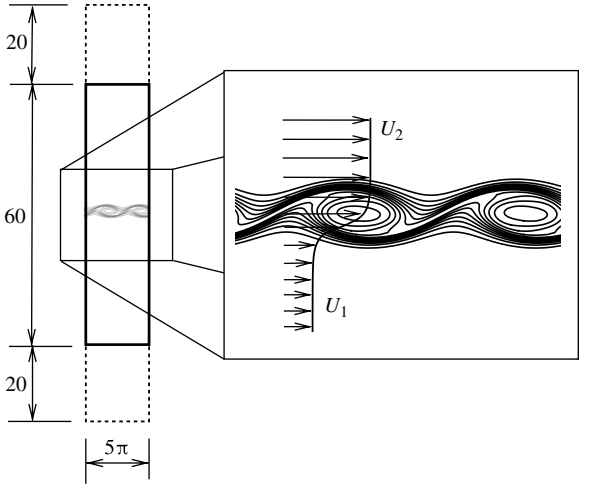


FIGURE 1. Schematic for the simulation of a two-dimensional shear layer.

As also shown in figure 1, a two-dimensional shear layer is simulated in a rectangular computational domain of $0 < x < 5\pi$ and $-50 < y < 50$ with 128×800 mesh points along x and y directions. Periodic boundary condition is applied along x. Along y, the physical domain has only $-30 < y < 30$ with the rest being buffer zones commonly used to mimic non-reflecting boundary conditions (Colonius, Lele & Moin 1993; Colonius *et al.* 1997; Freund 1997). The compressibility is characterized typically by convective Mach number (Bogdanoff 1983; Papamoschou & Roshko 1988)

$$M_c = \frac{U_2 - U_1}{2a_\infty}. \tag{3.1}$$

There is a total of five numerical simulations. The base case runs at Reynolds number $Re = 500$ and Mach number $M_c = 0.2$, and it provides the simulation data for most of the modelling effort. Then, there are four benchmark cases running at $M_c = 0.3$ and 0.4 for the same $Re = 500$, and $Re = 300$ and 1000 for the same $M_c = 0.2$. These benchmark cases are only used in § 5.4 to validate the model robustness and the ability to extend the model to 'off-design' Mach numbers and Reynolds numbers.

For initial velocity profile, we choose an incompressible self-similar solution similar to that derived by Schlichting & Gersten (2000):

$$u_s(\eta) = U_1 + \frac{U_2 - U_1}{2} erfc(-\eta), \quad v_s(\eta) = 0, \tag{3.2}$$

where the similarity variable η is given by

$$\eta = y\left(\frac{Re}{4(t - t_0)}\right)^{1/2}. \tag{3.3}$$

If the singularity time t_0 is set to $(-Re/4)$, there is $\eta = y$ at $t = 0$. If $U_1 = 0$ and $U_2 = 1$ are chosen, the initial velocity field for simulation is simply

$$u_0(y) = \tfrac{1}{2} erfc(-y), \quad v_0 = 0, \quad a_0 = 1. \tag{3.4}$$

https://doi.org/10.1017/jfm.2013.318 Published online by Cambridge University Press

There are two reasons for this choice of initial velocity profile: (i) it is an exact solution of incompressible Navier–Stokes equations; (ii) starting with the profile, an analytical solution (self-similar solution) exists for the viscous-damping-only case, which we can use to validate our low-dimensional model. However, the derivation of all model equations below including the evolution of the scaling variable has no prior knowledge of self-similarity, which preserves the generality of the current modelling effort. The initial profile is also used as a template function to evolve the scaling parameter dynamically, which will be discussed later in § 4.1.

To introduce the instability required for vortex roll-up and pairing, small perturbations with two streamwise wavenumbers (at $k = 1$ and $k = 2$) are added to the initial profile as

$$u = u_0 + A_f \mathrm{Re}[\hat{u_f} \exp(-\mathrm{i}\alpha_f x)] + A_s \mathrm{Re}[\hat{u_s} \exp(-\mathrm{i}\alpha_s x)] \tag{3.5}$$

$$v = v_0 + A_f \mathrm{Re}[\hat{v_f} \exp(-\mathrm{i}\alpha_f x)] + A_s \mathrm{Re}[\hat{v_s} \exp(-\mathrm{i}\alpha_s x)], \tag{3.6}$$

where the subscripts 'f' and 's' stand for the fundamental ($k = 2$) and subharmonic ($k = 1$) spatial frequencies, A is the small forcing amplitude for each frequency, $\hat{u}$ and $\hat{v}$ are the x- and y-direction components of the corresponding eigenfunctions computed from linear instability theory (Schmid & Henningson 2001; Drazin & Reid 2004), and $\alpha = 2\pi k/L$ corresponds to different spatial frequencies.

4. Low-dimensional models

4.1. *Mode decomposition*

POD has been widely used to provide bases for a new subspace to build models at lower dimension (Holmes *et al.* 1996). Later, modifications were introduced for special situations to improve the model efficiency in terms of the number of required POD modes to obtain similar or better model behaviour. Noack *et al.* (2003) added shift mode counting for the mean flow shifting. Rowley & Marsden (2000) applied the idea of symmetry reduction from geometric mechanics to factor out the slow travelling solution, which was generalized to other symmetry groups later (Rowley *et al.* 2003). For shear flows, it has been shown in our previous work on incompressible flows (Wei & Rowley 2009; Wei *et al.* 2012) that more efficient models can be achieved in a new space where the viscous growth of shear layers is removed through symmetry reduction. Here, a similar idea of constructing POD modes on a symmetry-reduced space is applied on compressible flows.

Knowing that the thickness of TD shear layers is spreading in time, we first scale all flow variables dynamically in the y direction as the shear layer evolving in time. With a vector of variable defined by $\boldsymbol{q} = (u, v, a)$ and a scaling factor $g(t) > 0$, we can define a new variable $\tilde{\boldsymbol{q}} = (\tilde{u}, \tilde{v}, \tilde{a})$ in the scaled space as

$$\tilde{\boldsymbol{q}}(x, g(t)y, t) = \boldsymbol{q}(x, y, t). \tag{4.1}$$

The scaling factor $g(t)$ is chosen to fit the flow the best with a preselected template function (Rowley *et al.* 2003). It is worth noting that the current definition of scaled variable is simpler than that used in the incompressible model (Wei & Rowley 2009), where a special coefficient matrix was added to re-enforce the divergence free condition for incompressibility. Choosing the initial velocity profile $\boldsymbol{q}_0 = (u_0, v_0, a_0)$ as

https://doi.org/10.1017/jfm.2013.318 Published online by Cambridge University Press

the template, we define $g(t)$ by

$$g(t) = \arg\min_{g} \left[\left\| u\left(x, \frac{y}{g}, t\right) - u_0 \right\|^2 + \left\| v\left(x, \frac{y}{g}, t\right) - v_0 \right\|^2 + \beta \left\| a\left(x, \frac{y}{g}, t\right) - a_0 \right\|^2 \right], \tag{4.2}$$

where $\beta = 2/\gamma(\gamma - 1)$ to match the current definition of total energy. L^2 norm is defined by an integration over space domain Ω with all y and the whole period 5π along x,

$$\| \cdot \|^2 = \int_{\Omega} (\cdot)^2 \, \mathrm{d}x \, \mathrm{d}y. \tag{4.3}$$

The scaling, with the purpose to remove the thickness growth, naturally define a new thickness δ_g as

$$\delta_g = 1/g(t). \tag{4.4}$$

Although they are mathematically different, δ_g is practically very close to the vorticity thickness δ_ω in all cases studied here, so that the use of δ_g and δ_ω is interchangeable for all of the qualitative discussion in this paper.

In the scaled space, the initial profile $\boldsymbol{q}_0 = (u_0, v_0, a_0)$ is almost identical to the time mean profile of $\tilde{\boldsymbol{q}}$. For convenience, let $\tilde{\boldsymbol{q}}_0 = \boldsymbol{q}_0$, so that the initial profile also plays the role of zero mode in the expansion of $\tilde{\boldsymbol{q}}$,

$$\tilde{\boldsymbol{q}}(x, y, t) = \tilde{\boldsymbol{q}}_0(y) + \sum_{j=1}^{\infty} a_j(t) \, \boldsymbol{\Phi}_j(x, y), \tag{4.5}$$

where $\boldsymbol{\Phi}_j$ are basis and a_j are the corresponding time coefficients. Applying the periodicity along x, we can further decouple the bases to Fourier modes in x and POD modes (in scaled space) in y. Thus, the expansion (4.5) becomes

$$\tilde{\boldsymbol{q}}(x, y, t) = \tilde{\boldsymbol{q}}_0(y) + \sum_{k=-\infty}^{+\infty} \sum_{n=0}^{\infty} a_{k,n}(t) \, \boldsymbol{\Phi}_{k,n}(x, y), \tag{4.6}$$

with

$$\boldsymbol{\Phi}_{k,n}(x, y) = \mathrm{e}^{2\pi \mathrm{i} k x / L} \boldsymbol{\phi}_{k,n}(y), \tag{4.7}$$

where k is the wavenumber index, L is the periodic domain length along x and $\boldsymbol{\phi}_{k,n}(y) = (\hat{u}_{k,n}, \hat{v}_{k,n}, \hat{a}_{k,n})$ is the nth POD mode for the kth wavenumber. To ensure that $\tilde{\boldsymbol{q}}$ is real, there is a constraint

$$\sum_{k=1}^{+M} \sum_{n=0}^{N} a_{k,n}(t) \, \boldsymbol{\Phi}_{k,n}(x, y) = \sum_{k=-M}^{-1} \sum_{n=0}^{N} a^*_{k,n}(t) \, \boldsymbol{\Phi}^*_{k,n}(x, y), \tag{4.8}$$

which will be applied later to simplify the model. The inner product used to define POD is now representing the total energy for compressible flows instead of kinetic energy only in traditional POD for incompressible flows:

$$\langle \tilde{\boldsymbol{q}}_1, \tilde{\boldsymbol{q}}_2 \rangle = \int_{\Omega} (\tilde{u}_1 \tilde{u}_2 + \tilde{v}_1 \tilde{v}_2 + \beta \tilde{a}_1 \tilde{a}_2) \, \mathrm{d}x \, \mathrm{d}y, \tag{4.9}$$

where $\tilde{\cdot}$ denotes the definition in scaled space, and the x integration is actually absorbed by orthogonality during the computation after each individual Fourier mode

https://doi.org/10.1017/jfm.2013.318 Published online by Cambridge University Press

is substituted in. The energy of each POD mode (k, n) is quantified by

$$\lambda_{k,n} = \overline{(\langle \tilde{\boldsymbol{q}} - \tilde{\boldsymbol{q}}_0,\ \boldsymbol{\Phi}_{k,n} \rangle)^2} = \overline{a_{k,n}^2}, \tag{4.10}$$

where $\bar{\cdot}$ denotes a time average. We need to point out that the inner product used here to compute POD modes is the same as that used later in Galerkin projection, unlike the case of the incompressible flow where two different inner products were used (Wei & Rowley 2009). So, the orthogonality of POD modes is now preserved when flow equations are projected onto these bases.

4.2. *Galerkin projection*

A general dynamical system is used at the beginning of our derivation, which is similar to the derivation used in the previous work on incompressible flows (Wei & Rowley 2009). However, the current scaling in (4.1) does not require any extra constraint on incompressibility. This change considerably simplifies the derivation and the final model equation. The dynamical system evolves on a function space H with the flow variable $\boldsymbol{q}$ at all points (x, y) in our spatial domain. The governing equation is

$$\frac{\partial \boldsymbol{q}(t)}{\partial t} = f(\boldsymbol{q}(t)), \tag{4.11}$$

where $\boldsymbol{q}(t) \in H$ is a snapshot of the entire flow at time t, f is a differential operator on H (e.g. all terms except the temporal term in the Navier–Stokes equations). If the scaling is noted by an operator $S_g : H \to H$, defined by

$$S_g[\boldsymbol{q}](x, y) = \boldsymbol{q}(x, gy), \quad \forall g \in \mathbb{R}^+, \tag{4.12}$$

the scaling (4.1) can be rewritten as $\boldsymbol{q}(t) = S_g[\tilde{\boldsymbol{q}}(t)]$, and the governing equation in terms of the scaled variable becomes

$$\frac{\partial}{\partial t} S_{g(t)}[\tilde{\boldsymbol{q}}(t)] = f(S_g[\tilde{\boldsymbol{q}}(t)]). \tag{4.13}$$

We manage to move the operator S_g outside of the time derivative as

$$\begin{aligned} \frac{\partial}{\partial t} S_{g(t)}[\tilde{\boldsymbol{q}}(t)](x, y) &= \frac{\partial}{\partial t} \tilde{\boldsymbol{q}}(x, g(t)y, t) \\ &= \frac{\partial \tilde{\boldsymbol{q}}}{\partial t}(x, gy, t) + \dot{g} y \frac{\partial \tilde{\boldsymbol{q}}}{\partial y}(x, gy, t) \\ &= S_g \left[\frac{\partial \tilde{\boldsymbol{q}}}{\partial t} \right](x, y) + \frac{\dot{g}}{g} S_g \left[y \frac{\partial \tilde{\boldsymbol{q}}}{\partial y} \right](x, y), \end{aligned} \tag{4.14}$$

then, equation (4.13) becomes

$$S_g \left[\frac{\partial \tilde{\boldsymbol{q}}}{\partial t} \right] = f(S_g[\tilde{\boldsymbol{q}}]) - \frac{\dot{g}}{g} S_g \left[y \frac{\partial \tilde{\boldsymbol{q}}}{\partial y} \right]. \tag{4.15}$$

Applying a reverse scaling operator $S_{1/g}$ on both sides of (4.15), we cancel some scaling operators and achieve

$$\frac{\partial \tilde{\boldsymbol{q}}}{\partial t} = f_g(\tilde{\boldsymbol{q}}) - \frac{\dot{g}}{g} y \frac{\partial \tilde{\boldsymbol{q}}}{\partial y}, \tag{4.16}$$

where $f_g(\tilde{\boldsymbol{q}}) = S_{1/g} f(S_g[\tilde{\boldsymbol{q}}])$. The new dynamic equation using the scaled variable $\tilde{\boldsymbol{q}}$ is similar to the original equation (4.11), with f being replaced by f_g, and with one additional term related to the scaling factor $g(t)$ and its rate of change.

https://doi.org/10.1017/jfm.2013.318 Published online by Cambridge University Press

Applying the above derivation to the isentropic Navier–Stokes equations in (2.1), where the function $f(\boldsymbol{q})$ is defined by

$$f(\boldsymbol{q}) = \boldsymbol{C}(\boldsymbol{q}, \boldsymbol{q}) + \frac{1}{Re}\boldsymbol{V}(\boldsymbol{q}), \tag{4.17}$$

with

$$\boldsymbol{C}(\boldsymbol{q}, \boldsymbol{q}) = \begin{pmatrix} -u\dfrac{\partial u}{\partial x} - v\dfrac{\partial u}{\partial y} - \beta\gamma a\dfrac{\partial a}{\partial x} \\ -u\dfrac{\partial v}{\partial x} - v\dfrac{\partial v}{\partial y} - \beta\gamma a\dfrac{\partial a}{\partial y} \\ -u\dfrac{\partial a}{\partial x} - v\dfrac{\partial a}{\partial y} - \dfrac{1}{\beta\gamma}a\left(\dfrac{\partial u}{\partial x} + \dfrac{\partial v}{\partial y}\right) \end{pmatrix} \tag{4.18a}$$

and

$$\boldsymbol{V}(\boldsymbol{q}) = \begin{pmatrix} \dfrac{\partial^2 u}{\partial x^2} + \dfrac{\partial^2 u}{\partial y^2} \\ \dfrac{\partial^2 v}{\partial x^2} + \dfrac{\partial^2 v}{\partial y^2} \end{pmatrix}, \tag{4.18b}$$

we can easily obtain $f_g(\tilde{\boldsymbol{q}})$ as

$$f_g(\tilde{\boldsymbol{q}}) = \boldsymbol{C}_g(\tilde{\boldsymbol{q}}, \tilde{\boldsymbol{q}}) + \frac{1}{Re}\boldsymbol{V}_g(\tilde{\boldsymbol{q}}), \tag{4.19}$$

with

$$\boldsymbol{C}_g(\tilde{\boldsymbol{q}}, \tilde{\boldsymbol{q}}) = \begin{pmatrix} -\tilde{u}\dfrac{\partial \tilde{u}}{\partial x} - g\tilde{v}\dfrac{\partial \tilde{u}}{\partial y} - \beta\gamma\tilde{a}\dfrac{\partial \tilde{a}}{\partial x} \\ -\tilde{u}\dfrac{\partial \tilde{v}}{\partial x} - g\tilde{v}\dfrac{\partial \tilde{v}}{\partial y} - \beta\gamma g\tilde{a}\dfrac{\partial \tilde{a}}{\partial y} \\ -\tilde{u}\dfrac{\partial \tilde{a}}{\partial x} - g\tilde{v}\dfrac{\partial \tilde{a}}{\partial y} - \dfrac{1}{\beta\gamma}\tilde{a}\left(\dfrac{\partial \tilde{u}}{\partial x} + g\dfrac{\partial \tilde{v}}{\partial y}\right) \end{pmatrix} \tag{4.20a}$$

and

$$\boldsymbol{V}_g(\tilde{\boldsymbol{q}}) = \begin{pmatrix} \dfrac{\partial^2 \tilde{u}}{\partial x^2} + g^2\dfrac{\partial^2 \tilde{u}}{\partial y^2} \\ \dfrac{\partial^2 \tilde{v}}{\partial x^2} + g^2\dfrac{\partial^2 \tilde{v}}{\partial y^2} \end{pmatrix}. \tag{4.20b}$$

Then, there is the same dynamic equation (4.16) for isentropic Navier–Stokes equations with above defined operators.

Starting with a simple model, we use only $k = \pm 1$, and the first two POD modes $n = 1$ and $n = 2$ for each wavenumber in the expansion of $\tilde{\boldsymbol{q}}$ in (4.6). With the constraint of (4.8), essentially, there are only two independent modes $\boldsymbol{\Phi}_{1,1}$ and $\boldsymbol{\Phi}_{1,2}$. Then, the summation becomes a finite truncation from the original $\tilde{\boldsymbol{q}}$. However, for simplicity, the notation $\tilde{\boldsymbol{q}}$ remains the same for the finite summation with no confusion. Using the same definition of inner product in the scaled space, we project (4.16) onto

https://doi.org/10.1017/jfm.2013.318 Published online by Cambridge University Press

the basis functions as

$$\left\langle \frac{\partial \tilde{\boldsymbol{q}}}{\partial t},\, \boldsymbol{\Phi}_{k,n} \right\rangle = \langle \boldsymbol{C}_g(\tilde{\boldsymbol{q}}, \tilde{\boldsymbol{q}}),\, \boldsymbol{\Phi}_{k,n} \rangle + \frac{1}{Re} \langle \boldsymbol{V}_g(\tilde{\boldsymbol{q}}),\, \boldsymbol{\Phi}_{k,n} \rangle + \left\langle -\frac{\dot{g}}{g} y \frac{\partial \tilde{\boldsymbol{q}}}{\partial y},\, \boldsymbol{\Phi}_{k,n} \right\rangle. \quad (4.21)$$

Substituting the orthogonal modes $\boldsymbol{\Phi}_{1,1}$ and $\boldsymbol{\Phi}_{1,2}$ in above equation, we get the final dynamic equation for the coefficient vector $\boldsymbol{a} = (a_{1,1}\, a_{1,2})^{\mathrm{T}}$:

$$\dot{\boldsymbol{a}} = \left(\boldsymbol{B} + \frac{1}{Re} \boldsymbol{D} + \frac{\dot{g}}{g} \boldsymbol{E} \right) \boldsymbol{a}, \quad (4.22)$$

where matrices $\boldsymbol{B}$, $\boldsymbol{D}$ and $\boldsymbol{E}$ are defined by

$$\boldsymbol{B} = \begin{bmatrix} b_{11} + gc_{11} & b_{12} + gc_{12} \\ b_{21} + gc_{21} & b_{22} + gc_{22} \end{bmatrix}, \quad (4.23a)$$

$$\boldsymbol{D} = \begin{bmatrix} -(2\pi/L)^2 (n_{11}) + g^2 d_{11} & -(2\pi/L)^2 (n_{12}) + g^2 d_{12} \\ -(2\pi/L)^2 (n_{21}) + g^2 d_{21} & -(2\pi/L)^2 (n_{22}) + g^2 d_{22} \end{bmatrix}, \quad (4.23b)$$

$$\boldsymbol{E} = \begin{bmatrix} e_{11} & e_{12} \\ e_{21} & e_{22} \end{bmatrix}, \quad (4.23c)$$

with constant coefficients, which depend only on basis functions and are defined in appendix B. In comparison with the previous work on an incompressible model (Wei & Rowley 2009), the current compressible model is in a much simpler form because of two major advantages: (i) simple scaling operation; and (ii) consistent definition of the inner product for POD and Galerkin projection.

4.3. *Equations of motion for the thickness*

Since there is no prior knowledge of the scaling, we need one more dynamic equation for the scaling variable $g(t)$ to close the system. Following (4.2), the condition that $\tilde{\boldsymbol{q}}$ be scaled so that it most closely matches $\boldsymbol{q}_0$ may be written as

$$\left.\frac{\mathrm{d}}{\mathrm{d}s}\right|_{s=0} \|\tilde{u}(x, y, t) - u_0(h(s)y)\|^2 + \|\tilde{v}(x, y, t) - v_0(h(s)y)\|^2 + \beta \|\tilde{a}(x, y, t) - a_0(h(s)y)\|^2 = 0, \quad (4.24)$$

where $h(s)$ is any curve in $\mathbb{R}^+$ with $h(0) = 1$, and $\|\cdot\|^2$ is the same norm as before on the space of functions of (x, y): that is, $h = 1$ is a local minimum of the error norm above. We have then

$$-2 \left\langle \left.\frac{\mathrm{d}}{\mathrm{d}s}\right|_{s=0} u_0(h(s)y), \tilde{u}(x, y, t) - u_0(y) \right\rangle - 2 \left\langle \left.\frac{\mathrm{d}}{\mathrm{d}s}\right|_{s=0} v_0(h(s)y), \tilde{v}(x, y, t) - v_0(y) \right\rangle - 2\beta \left\langle \left.\frac{\mathrm{d}}{\mathrm{d}s}\right|_{s=0} a_0(h(s)y), \tilde{a}(x, y, t) - a_0(y) \right\rangle = 0, \quad (4.25)$$

which becomes

$$\left\langle y \frac{\partial u_0}{\partial y}, \tilde{u} - u_0 \right\rangle + \left\langle y \frac{\partial v_0}{\partial y}, \tilde{v} - v_0 \right\rangle + \beta \left\langle y \frac{\partial a_0}{\partial y}, \tilde{a} - a_0 \right\rangle = 0. \quad (4.26)$$

https://doi.org/10.1017/jfm.2013.318 Published online by Cambridge University Press

Since v_0, $\partial v_0/\partial y$ and $\partial a_0/\partial y$ are all zeros for the chosen template, the above equation is simplified to

$$\left\langle y\frac{\partial u_0}{\partial y}, \tilde{u} - u_0 \right\rangle = 0, \tag{4.27}$$

where a simple inner product for the scalar is used as

$$\langle a, b\rangle = \int_{\Omega} (ab)\,\mathrm{d}x\,\mathrm{d}y. \tag{4.28}$$

A time differentiation of (4.27) leads to

$$\left\langle y\frac{\partial u_0}{\partial y}, \frac{\partial \tilde{u}}{\partial t} \right\rangle = 0. \tag{4.29}$$

If (4.16) is written separately in $\tilde{u}$, $\tilde{v}$ and $\tilde{a}$ as

$$\frac{\partial \tilde{u}}{\partial t} = f_g^1(\tilde{u}) - \frac{\dot{g}}{g} y\frac{\partial \tilde{u}}{\partial y} \tag{4.30a}$$

$$\frac{\partial \tilde{v}}{\partial t} = f_g^2(\tilde{v}) - \frac{\dot{g}}{g} y\frac{\partial \tilde{v}}{\partial y} \tag{4.30b}$$

$$\frac{\partial \tilde{a}}{\partial t} = f_g^2(\tilde{a}) - \frac{\dot{g}}{g} y\frac{\partial \tilde{a}}{\partial y}, \tag{4.30c}$$

using the first equation of (4.30*a*), we have

$$\left\langle y\frac{\partial u_0}{\partial y}, f_g^1(\tilde{u}) - \frac{\dot{g}}{g} y\frac{\partial \tilde{u}}{\partial y} \right\rangle = 0, \tag{4.31}$$

and, then,

$$\frac{\dot{g}}{g} = \frac{\langle f_g^1(\tilde{u}), y\partial_y u_0\rangle}{\langle y\partial_y \tilde{u}, y\partial_y u_0\rangle}. \tag{4.32}$$

Applying the equation on two modes $\boldsymbol{\Phi}_{1,1}$ and $\boldsymbol{\Phi}_{1,2}$ for a finite truncation of $\tilde{u}$, we get the evolution equation of scaling variable g for single-frequency (two-mode) model:

$$\dot{g} = \frac{r_{11}}{n_0} a_{1,1} a_{1,1}^* g + \frac{r_{22}}{n_0} a_{1,2} a_{1,2}^* g + \frac{r_{21}}{n_0} a_{1,1} a_{1,2}^* g + \frac{r_{12}}{n_0} a_{1,2} a_{1,1}^* g + \frac{1}{Re}\frac{d_0}{n_0} g^3, \tag{4.33}$$

where all constant coefficients are defined in appendix B.

If we add two more modes $n = 1$ and 2 for wavenumber index $k = 2$, the same derivation yields the equations for g, $a_{1,1}$, $a_{1,2}$, $a_{2,1}$ and $a_{2,2}$ to describe more complex physics. The resulting equations are lengthy, however, and are listed in appendix C.

5. Results and discussion

We choose the case with convective Mach number $M_c = 0.2$ and Reynolds number $Re = 500$ as a base case to compare the compressible low-dimensional model proposed in this paper to the previous incompressible model (Wei & Rowley 2009) and the direct numerical simulation. Then, the model derived from the base-case database is challenged by 'off-design' parameters: (i) different Mach numbers at $M_c = 0.3$ and 0.4; and (ii) different Reynolds numbers at 300 and 1000.

https://doi.org/10.1017/jfm.2013.318 Published online by Cambridge University Press

5.1. *Flow without perturbation*

For the flow with the velocity profile defined in (3.4) with no perturbations added, at the incompressible limit, the dynamics should follow the self-similar solution

$$u(y,t) = u_0(\eta(y,t)), \quad v = 0, \tag{5.1}$$

with $\eta(y,t)$ given by (3.3) with $t_0 = -Re/4$. The same solution can be recovered by our compressible model with no self-similarity being assumed.

Without initial perturbation, all POD coefficients in '$\boldsymbol{a}$' remain zero, and there left only one equation (4.33), which is simplified to

$$\dot{g} = \frac{1}{Re}\frac{d_0}{n_0}g^3. \tag{5.2}$$

Substituting u_0 from (3.4) into the equations for n_0 and d_0 in appendix B, we have

$$n_0 = \frac{1}{\pi}\int y^2 \exp(-2y^2)\,\mathrm{d}y, \tag{5.3a}$$

$$d_0 = -\frac{2}{\pi}\int y^2 \exp(-2y^2)\,\mathrm{d}y, \tag{5.3b}$$

and (5.2) therefore reduces to

$$\dot{g} = -\frac{2}{Re}g^3. \tag{5.4}$$

Solving (5.4) with initial condition $g(0) = 1$ gives

$$g(t) = \left(\frac{Re}{4t + Re}\right)^{1/2}. \tag{5.5}$$

Compared with the definition of $\eta(y,t)$ in (3.3), we can easily observe the following relation

$$g(t) = \frac{\eta(t)}{y}. \tag{5.6}$$

With no perturbation, equations (4.1) and (4.6) indicate a solution

$$u(x,y,t) = u_0(g(t)y), \quad v = 0, \tag{5.7}$$

which is identical to the analytical solution in (5.1) by substituting the relation (5.6). It is no surprise that there is the same conclusion for the no-perturbation incompressible solution derived by Wei & Rowley (2009). When the initial profile has only u_0 being non-zero and there is no initial perturbation, the compressible and incompressible models reduce to the same (5.4) for g.

5.2. *Flow with a single wavenumber: $k = 1$ perturbation*

Then, the initial perturbation with only a single wavenumber, $k = 1$, is considered for the flow and model. Figure 2 shows the y component of the corresponding eigenfunction of $k = 1$, which is directly computed from the Orr–Sommerfeld equation (Schmid & Henningson 2001). However, both $\hat{v}$ and $\hat{u}$ (from the continuity equation) are seeded with very small amplitude ($\sim 0.008 a_\infty$) to initiate the instability.

The time evolution of the shear layer vorticity thickness computed by numerical simulation is shown in figure 3, where three developing stages are identified: (1) the

https://doi.org/10.1017/jfm.2013.318 Published online by Cambridge University Press

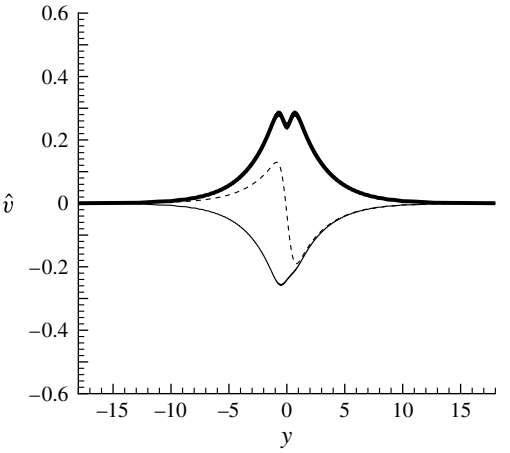


FIGURE 2. Plot of $\hat{v}$ of the most unstable mode for $k = 1$. The thin solid line represents the real value, the thin dashed line represents the imaginary value and the thick solid line represents the absolute value.

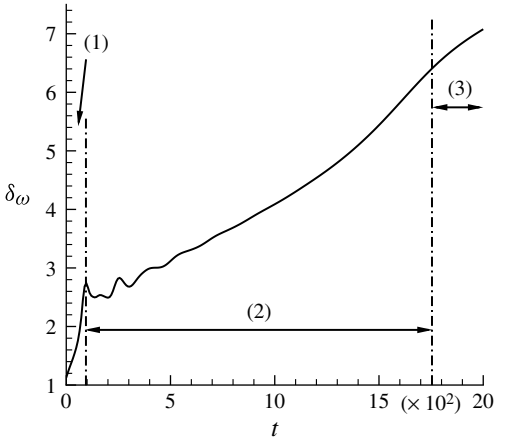


FIGURE 3. Vorticity thickness δ_ω (from numerical simulation) for flow with $k = 1$ perturbation for $M_c = 0.2$ case: three developing stages are marked, corresponding to (1) the growth of instability, (2) nonlinear saturation and (3) pure viscous dissipation.

rapid thickness growth by the roll-up of vortices at wavenumber $k = 1$; (2) the stabilization and transition by nonlinear saturation and viscous dissipation; (3) pure viscous dissipation.

POD applied in the scaled space shows an obvious advantage in energy capture, which is shown in table 1. Throughout the paper, each Fourier-POD mode is referred to as mode (k, n) (e.g. mode $(1, 2)$ for the $n = 2$ POD mode of wavenumber $k = 1$). It is shown that mode $(1, 1)$ contains most of the energy (92.8 %) while modes $(1, 2)$ and $(2, 1)$ share most of the rest. All POD modes of $k = 0$ contribute to only 0.8 %, which benefits from the successful scaling of mean flow to remove its spreading in time. Although modes $(1, 2)$ and $(2, 1)$ have similar energy levels, in practice, mode

https://doi.org/10.1017/jfm.2013.318 Published online by Cambridge University Press

(k, n)	λ	Energy (%)
(1, 1)	119.3	92.8
(1, 2)	3.9	3.0
(2, 1)	3.6	2.8
All $k = 0$		0.8

TABLE 1. Energy contained in different Fourier-POD modes for the flow with initial perturbation at $k = 1$.

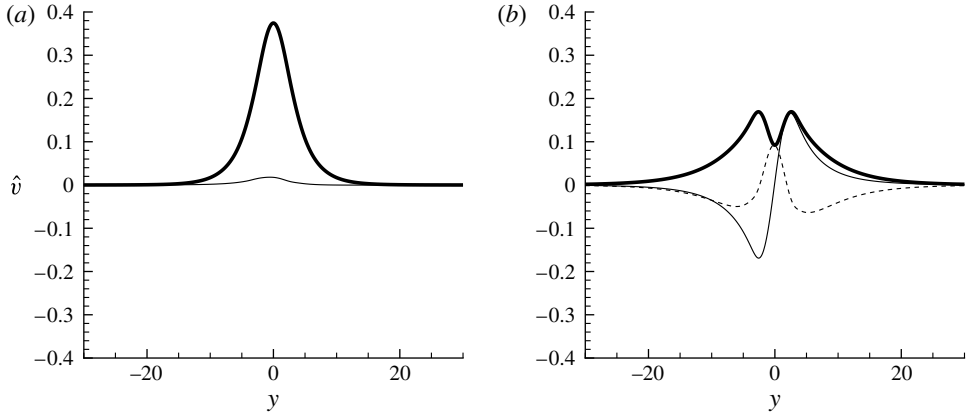


FIGURE 4. Plot of $\hat{v}$ of POD modes (*a*) $(k, n) = (1, 1)$ and (*b*) $(k, n) = (1, 2)$. The thin solid line represents the real value, the thin dashed line represents the imaginary value and the thick solid line represents the absolute value.

(1, 2) is dynamically important and kept, and mode (2, 1) has a negligible impact on the overall dynamics and therefore is ignored in the single-frequency model. The importance of POD mode (1, 2) may be indicated by its shape as shown in figure 4. In a comparison with the instability mode at $k = 1$ (figure 2), we argue that the dip at the centre of mode (1, 2) is critical in creating the overall shape of the instability mode (also with a dip at the centre) which helps to sustain proper instability. This hypothesis is meant to be qualitative because of the obvious difference in definition and assumption between POD modes and instability modes. Similar POD modes and energy budgets have been observed in the incompressible model by Wei & Rowley (2009), although the definitions of both inner product and scaling are different in the current paper.

With the POD modes being substituted in (4.22) and (4.33), which have coefficients defined in (4.23) and the detailed equations in appendix B, the model results are shown in figure 5. Figure 5(*a*), which is considered exact, shows the history of coefficients a_{11} and a_{12} calculated by a direct projection from the simulation data. Here and for the rest of the paper, only the real part of complex coefficients $a_{k,n}$ is plotted; the imaginary part behaves similarly. The thickness δ_g is also calculated directly from the simulation data as defined by (4.2) and (4.4). Figure 5(*b*) is the model result, which predicts well the history of both coefficients and thickness growth. All three dynamic stages (i.e. roll-up, transition and viscous damping) are clearly predicted while the thickness is somewhat overestimated at the end of roll-up. For

https://doi.org/10.1017/jfm.2013.318 Published online by Cambridge University Press

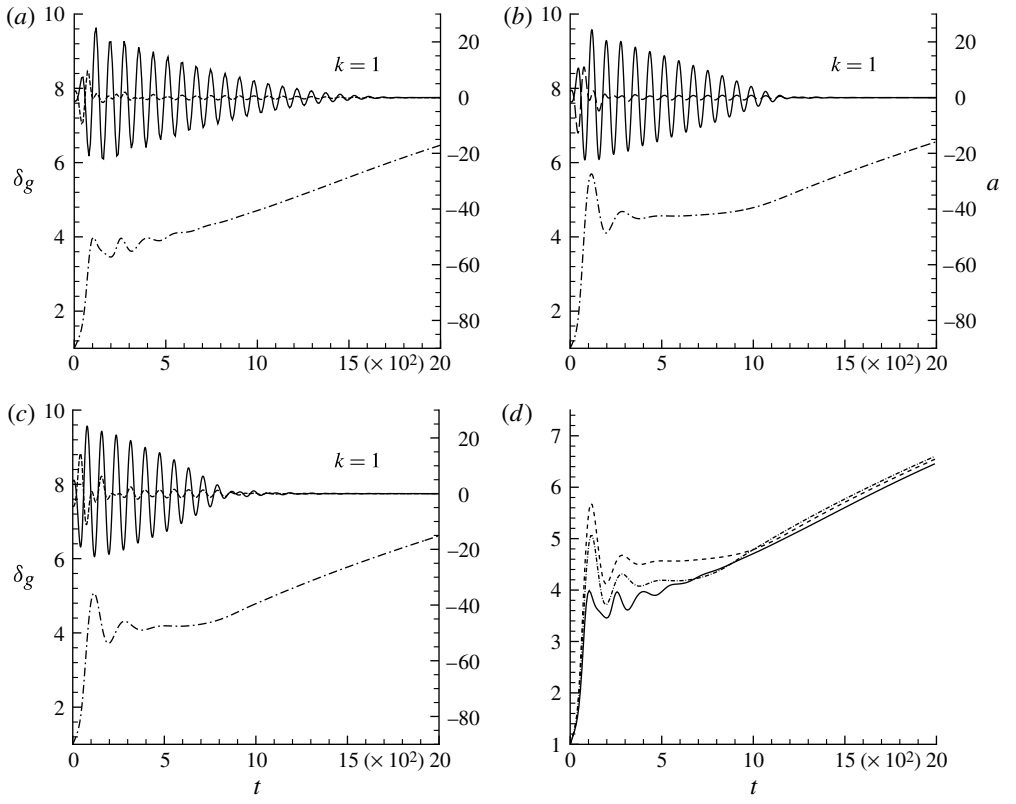


FIGURE 5. Comparison of dynamic behaviour of the flow with $k = 1$ initial perturbation: (*a*) direct projection and results from numerical simulation of compressible Navier–Stokes equations; (*b*) compressible model; (*c*) incompressible model (Wei & Rowley 2009). Here: ——, time coefficients $a_{11}(t)$; − − −−, time coefficients $a_{12}(t)$; and − · − · −, shear layer thickness δ_g. (*d*) Comparison of the thickness growth computed from direct numerical simulation (——), the compressible model (− − − −) and the incompressible model (− · − · −).

comparison, the result from the incompressible model (Wei & Rowley 2009) is shown in figure 5(*c*). The modes are dissipated at a slightly faster rate in the incompressible model, and the overestimation of the thickness is slightly less. The prediction of thickness growth is compared more closely in figure 5(*d*) with all three of them plotted against each other. Overall, the compressible model and incompressible model have similar performance in the description of single-frequency dynamics.

5.3. *Flow with double wavenumbers: $k = 1$ and $k = 2$ perturbations*

The introduction of both $k = 1$ and $k = 2$ allows more complex dynamics such as vortex pairing/merging and mode competition between the fundamental and the subharmonic frequencies. To introduce the instability, only a small perturbation ($\sim 0.008 a_\infty$) with the fundamental wavenumber $k = 2$ is seeded. The instability mode at $k = 2$ (figure 6) is used to define the perturbation. The current subharmonic $k = 1$ is started by numerical noise, then takes off through nonlinear interaction with the fundamental and as it becomes more unstable at larger shear layer thickness.

https://doi.org/10.1017/jfm.2013.318 Published online by Cambridge University Press

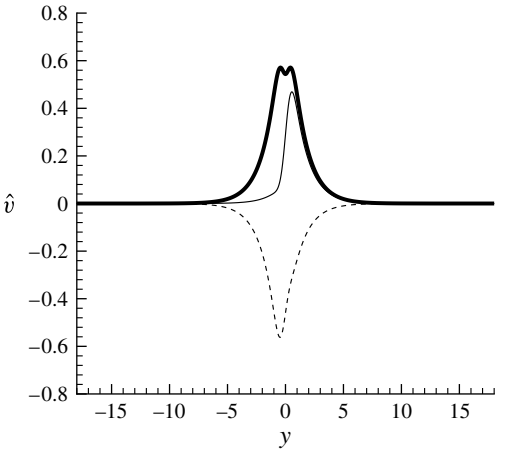


FIGURE 6. Plot of $\hat{v}$ of the most unstable mode for $k = 2$. The thin solid line represents the real value, the thin dashed line represents the imaginary value and the thick solid line represents the absolute value.

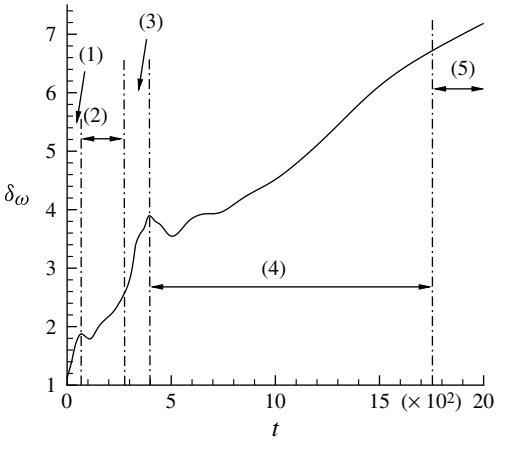


FIGURE 7. Vorticity thickness δ_ω (from numerical simulation), with an initial $k = 2$ perturbation for $M_c = 0.2$ case: five stages in the development are marked (see the text for a description).

Reasonably, we expect a four-mode model with two POD modes for each wavenumber to capture the more complex dynamics, which is depicted as five stages in figure 7: (1) the rapid thickness growth by the roll-up of vortices at the fundamental wavenumber $k = 2$; (2) the stabilization of the fundamental; (3) the rapid thickness growth by the pairing of vortices as the subharmonic wavenumber $k = 1$ takes over to be the most unstable mode; (4) the stabilization and transition by nonlinear saturation and viscous dissipation; (5) pure viscous dissipation.

The superior energy captured by POD modes in the scaled space remains, and this time, it is shared between the first POD modes of $k = 1$ (67.4 %) and $k = 2$ (27.4 %) as shown in table 2. The individual POD modes are shown in figure 8. For the same

https://doi.org/10.1017/jfm.2013.318 Published online by Cambridge University Press

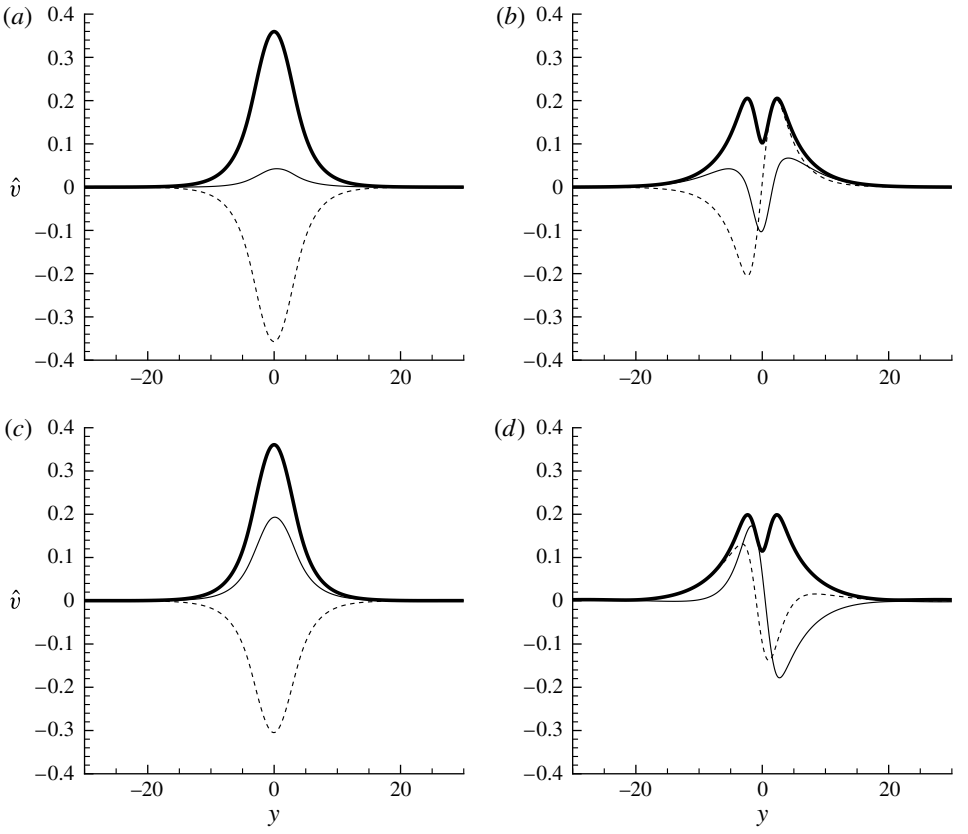


FIGURE 8. Plots of $\hat{v}$ of POD modes (*a*) $(k, n) = (1, 1)$, (*b*) $(k, n) = (1, 2)$, (*c*) $(k, n) = (2, 1)$ and (*d*) $(k, n) = (2, 2)$. The thin solid lines represent the real value, the thin dashed lines represent the imaginary value and the thick solid lines represent the absolute value.

(k, n)	λ	Energy (%)
(1, 1)	24.7	67.4
(2, 1)	10.1	27.4
(1, 2)	0.8	2.1
(2, 2)	0.6	1.5
All $k = 0$		0.3

TABLE 2. Energy contained in different Fourier-POD modes for the flow with both the fundamental ($k = 2$) and the subharmonic ($k = 1$).

reason mentioned earlier, the second POD modes at both wavenumbers need to be kept to sustain proper instability, although their energy contributions are small.

Substituting these four POD modes into the model equations and coefficients in appendix C, we compare the model results with the exact solution from numerical simulation and the previous incompressible model (Wei & Rowley 2009) in figure 9. The direct projection from the simulation data (figure 9*a*) shows that the coefficients

https://doi.org/10.1017/jfm.2013.318 Published online by Cambridge University Press

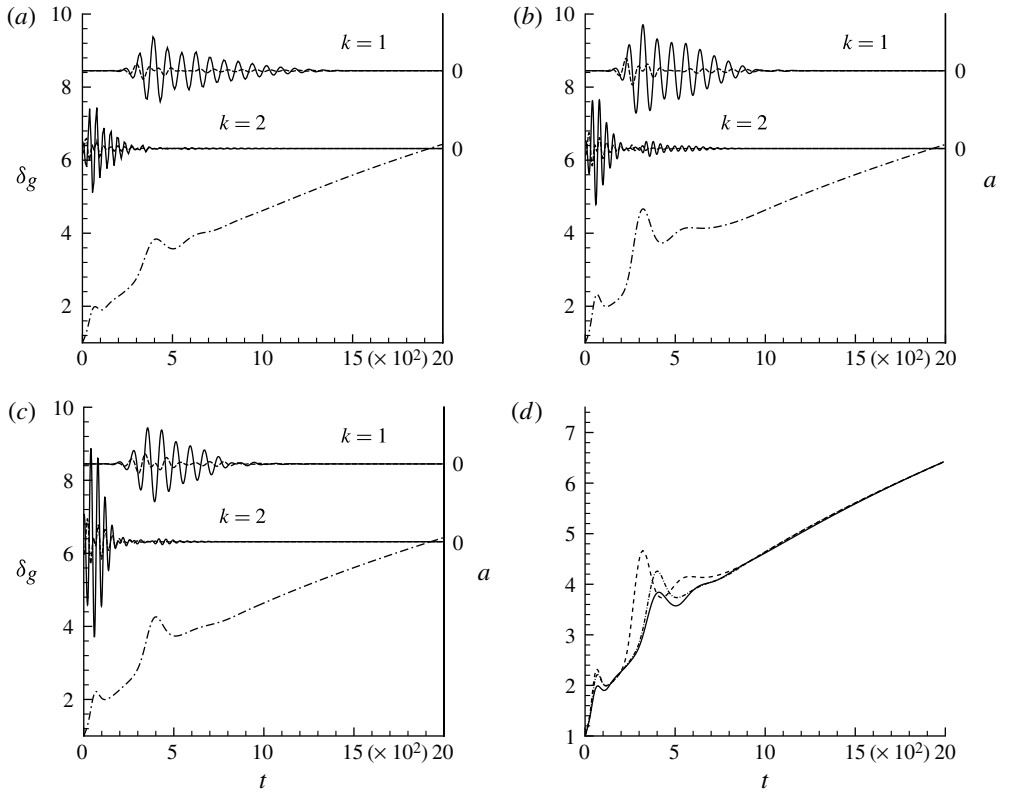


FIGURE 9. Comparison of the dynamic behaviour of the flow with both $k = 1$ and $k = 2$: (*a*) 'exact solution' from the numerical simulation of compressible Navier–Stokes equations; (*b*) compressible model; (*c*) incompressible model (Wei & Rowley 2009). Here: ——, time coefficients $a_{11}(t)$ and $a_{21}(t)$; – – ––, time coefficients $a_{12}(t)$ and $a_{22}(t)$; and – · – · –, shear layer thickness δ_g. (*d*) Comparison of the thickness growth computed from direct numerical simulation (——), the compressible model (– – – –) and the incompressible model (–·–·–). The same scale is used for coefficients a in the comparison.

at the fundamental $k = 2$ and the subharmonic $k = 1$ change the dominant role as the shear layer thickness grows. The switch between the modes aligns with the switch of the most unstable modes as the shear layer gets thicker. The role of 'base flow' in such a switch of the dominant frequency has also been reported in the low-dimensional model of a high-lift configuration by Luchtenburg *et al.* (2009) in a different scenario. As vortex dynamics is concerned, the behaviour of mode coefficients and thickness marks the vortex roll-up (i.e. the appearance of $k = 2$), vortex pairing/marging (i.e. the transition from $k = 2$ to $k = 1$) and the saturation and dissipation. The current compressible model successfully reproduces the behaviour of all four modes and the change of shear layer thickness in all five developing stages (figure 9*b*). Again, the performance of the compressible model is comparable with the incompressible model (figure 9*c*) and they both reproduce the simulation result well (figure 9*d*). It is worth noting that with comparable accuracy the current compressible model is simpler (by keeping the orthogonality) and allows the consideration of the compressibility (e.g. Mach number effect).

https://doi.org/10.1017/jfm.2013.318 Published online by Cambridge University Press

5.4. *Model robustness and adaptation*

The robustness of the compressible model is challenged by varying the Mach number and Reynolds number as parameters of the model built from the base case ($M_c = 0.2$ and $Re = 500$) and comparing the results against the numerical simulations at new parameters and the models based on new simulation data. Below, we first consider different Mach numbers $M_c = 0.3$ and 0.4 (with the same $Re = 500$), then different Reynolds numbers $Re = 300$ and 1000 (with the same $M_c = 0.2$). The practice of extending reduced-order models to new parametric space from the original simulation is also known as model adaptation (Amsallem & Farhat 2008).

5.4.1. *Extension in Mach number*

Using a_∞ as a universal characteristic speed prevents the Mach number M_c from appearing directly in the governing equation (2.1) and the derived model equations. Instead, different M_c of the shear flow is achieved through the implementation of a different mean flow with U_1 and U_2 which define the Mach number in (3.1). Using the mean flow and POD modes from the base case ($M_c = 0.2$ and $Re = 500$), we obtain a native model for $M_c = 0.2$. Simply stretching the mean flow proportionally to reach $M_c = 0.3$ and 0.4 and still using old POD modes of $M_c = 0.2$, we can recalculate model coefficients and adapt the model for the new Mach numbers without additional numerical simulation at the new parameters. The adapted models at $M_c = 0.3$ and 0.4 are plotted in figure 10. The models remain stable when they are extended to these Mach numbers. For benchmarking purposes, in parallel, we run numerical simulations at $M_c = 0.3$ and 0.4 and obtain native models (i.e. new mean flow and new POD modes from the corresponding simulations) at these Mach numbers. The template for native models is chosen in the same way, where the initial flow being stretched respectively for each Mach number is used. The native models are also plotted in figure 10. In this comparison, the difference between the adapted model and the native model is very subtle for both new Mach numbers. The thickness growth predicted by both native and adapted models matches well with the result from direct numerical simulation data marked by a thick solid line in the same figure.

Furthermore, as shown in figure 11, different developing histories of the shear layer thickness at different Mach numbers are compared to show the compressibility effects, in the same way as in the work by Sandham & Reynolds (1990). More importantly, the current comparison includes the results from direct numerical simulation (figure 11*a*), the native models (figure 11*b*) and the adapted models (figure 11*c*). Using the time scale based on the speed of sound, we clearly see that the increase in Mach number promotes the appearance of both the vortex roll-up (i.e. the first peak of thickness in the figure) and pairing/merging (i.e. the second peak). Such trend is consistently captured by both native and adapted models. This observation does not contradict with the results of Sandham & Reynolds (1990) and Sandham (1994) for temporal developing shear layers and Day, Mansour & Reynolds (2001) for spatial developing shear layers, where they showed instead a delay of the appearance of the vortex roll-up by the increase of convective Mach number. In their results, the time is scaled by shear layer velocity instead of the sound speed. In figure 12, we plot our current results in the same non-dimensional time as the references, the peak of vortex roll-up, in fact, appears as being delayed at higher Mach number. Again, the same trend is successfully captured by both native and adapted models.

5.4.2. *Extension in Reynolds number*

The extension in Reynolds number is more straightforward as it appears explicitly in the governing equations and models. Using the model of the base case ($M_c = 0.2$

https://doi.org/10.1017/jfm.2013.318 Published online by Cambridge University Press

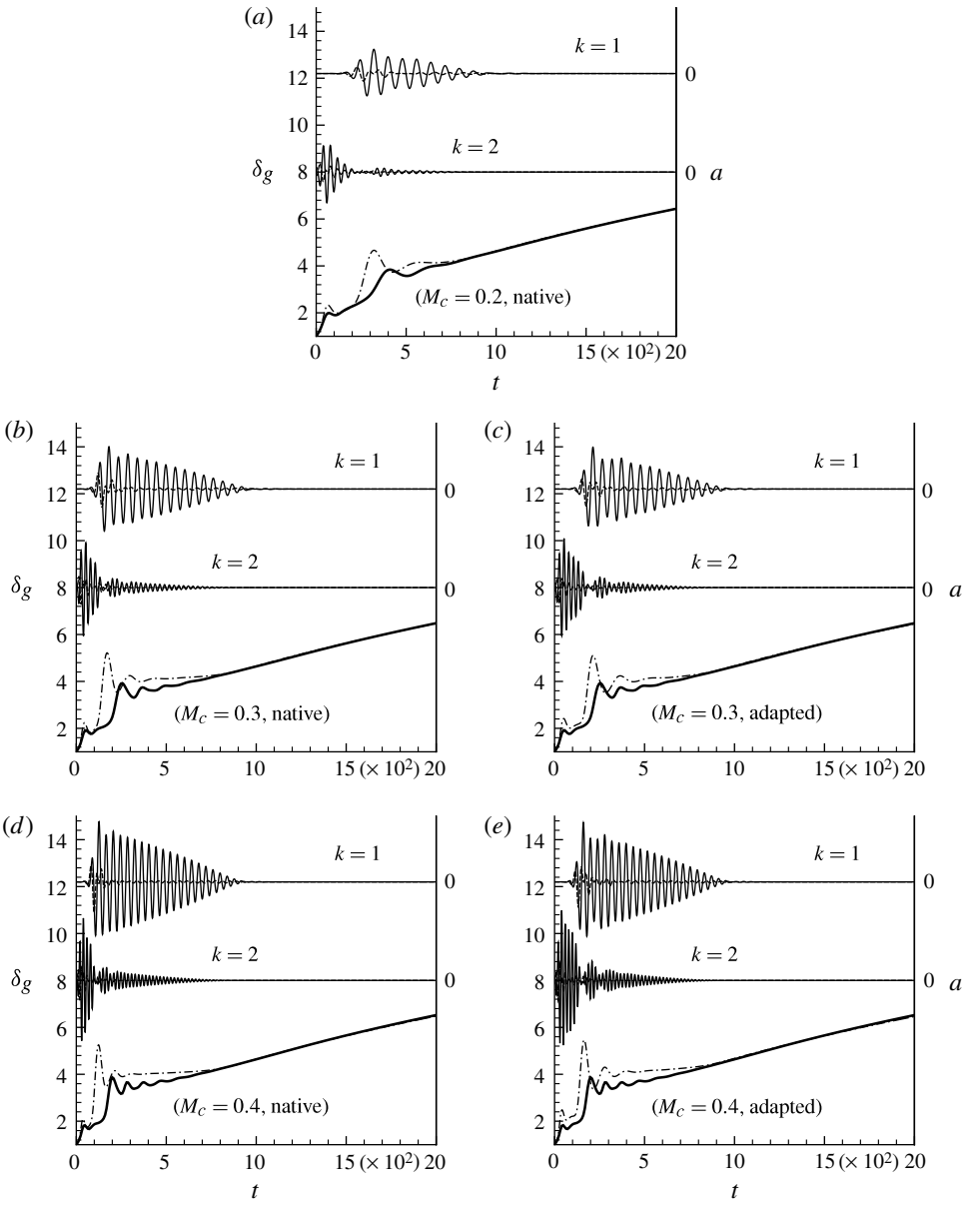


FIGURE 10. Comparison of native models and adapted models for the extension of Mach number from $M_c = 0.2$ to $M_c = 0.3$ and 0.4. Here: ——, time coefficients $a_{11}(t)$ and $a_{21}(t)$; − − ——, time coefficients $a_{12}(t)$ and $a_{22}(t)$; and − · − · −, the shear layer thickness δ_g (for comparison, —— is marked for the thickness computed from direct numerical simulation data at corresponding Mach numbers). The same scale is used for coefficients a in the comparison.

and $Re = 500$), we change the Reynolds number directly to 300 and 1000 to achieve adapted models without extra simulation. For benchmarking purposes, we also run two simulations at $Re = 300$ and $Re = 1000$ and build native models using new simulation data. It is worth mentioning that the new simulations have the same initial flow which

https://doi.org/10.1017/jfm.2013.318 Published online by Cambridge University Press

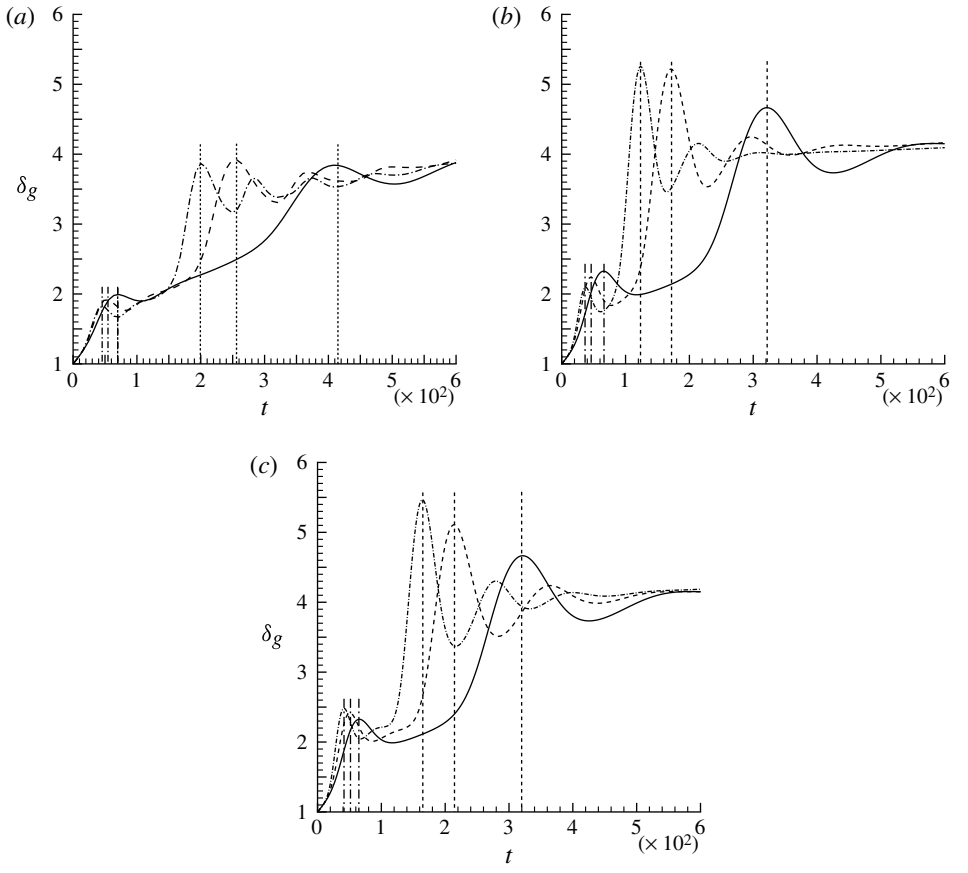


FIGURE 11. Developing history of the shear layer thickness δ_g at different convective Mach numbers M_c: (*a*) by direct numerical simulation; (*b*) by native models; (*c*) by adapted models using the same database at $M_c = 0.2$. Here: ——, $M_c = 0.2$; − − −−, $M_c = 0.3$; and − · − · −, $M_c = 0.4$.

implies the same mean flow in the scaled space and the same template for building native models under different Reynolds numbers.

As shown in figure 13, the models remain stable for 'off-design' Reynolds numbers, and the adapted models without new simulation match surprisingly well with the simulation and native models. The Reynolds number effect shown by all models is consistent with experimental and numerical observations: at low Reynolds number, perturbations are largely suppressed by viscosity and the main character of shear layer is viscous dissipation; at high Reynolds number, perturbations are promoted at both frequencies and result in stronger nonlinear interaction. For comparison, the thickness growth computed from direct simulation data is marked by thick solid lines in the same figure. Both native and adapted models successfully predict the thickness growth and fluctuation over the entire range from low to high Reynolds numbers.

The extension to 'off-design' Reynolds number has previously been discussed by Deane *et al.* (1991) in their low-dimensional models of grooved channel flow and circular cylinder flow. Their models were based on traditional POD-Galerkin projection and could not be extended to other Reynolds number directly. However, they made the

https://doi.org/10.1017/jfm.2013.318 Published online by Cambridge University Press

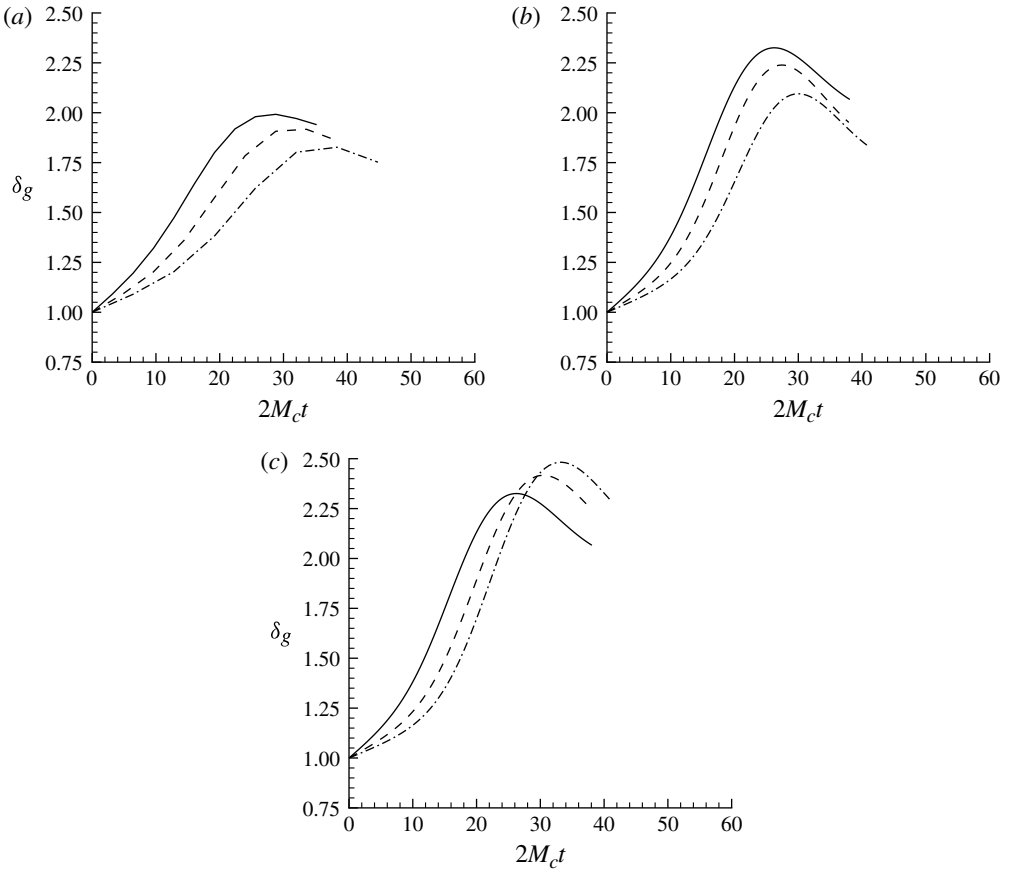


FIGURE 12. Developing history of the shear layer thickness δ_g with new time scale at different convective Mach numbers M_c: (*a*) by direct numerical simulation; (*b*) by native models; (*c*) by adapted models using the same database at $M_c = 0.2$. Here: ——, $M_c = 0.2$; – – ––, $M_c = 0.3$; and – · – · –, $M_c = 0.4$.

model extension work by tuning empirically the mean-flow thickness in the model to match the simulation data at the new Reynolds number. Our current models, on the other hand, do not require any empirical modification to work on 'off-design' Mach numbers and Reynolds numbers. This difference can be explained by the inclusion of a separate dynamic equation for the scaling variable $g(t)$, which is capable of automatic adjustment of the mean-flow thickness with respect to new flow parameters and the corresponding dynamics of base modes. Thus, it suggests that the current model may work at other 'off-design' parameters if the effects of those parameters are mainly through the change of mean flow.

6. Conclusions

The modelling is based on the isentropic Navier–Stokes equations, which are adopted as an approximation of the compressible Navier–Stokes equations used in the simulation of TD compressible shear layers. This choice provides a well-defined inner product to represent the total energy of weakly compressible flows. Then, for

https://doi.org/10.1017/jfm.2013.318 Published online by Cambridge University Press

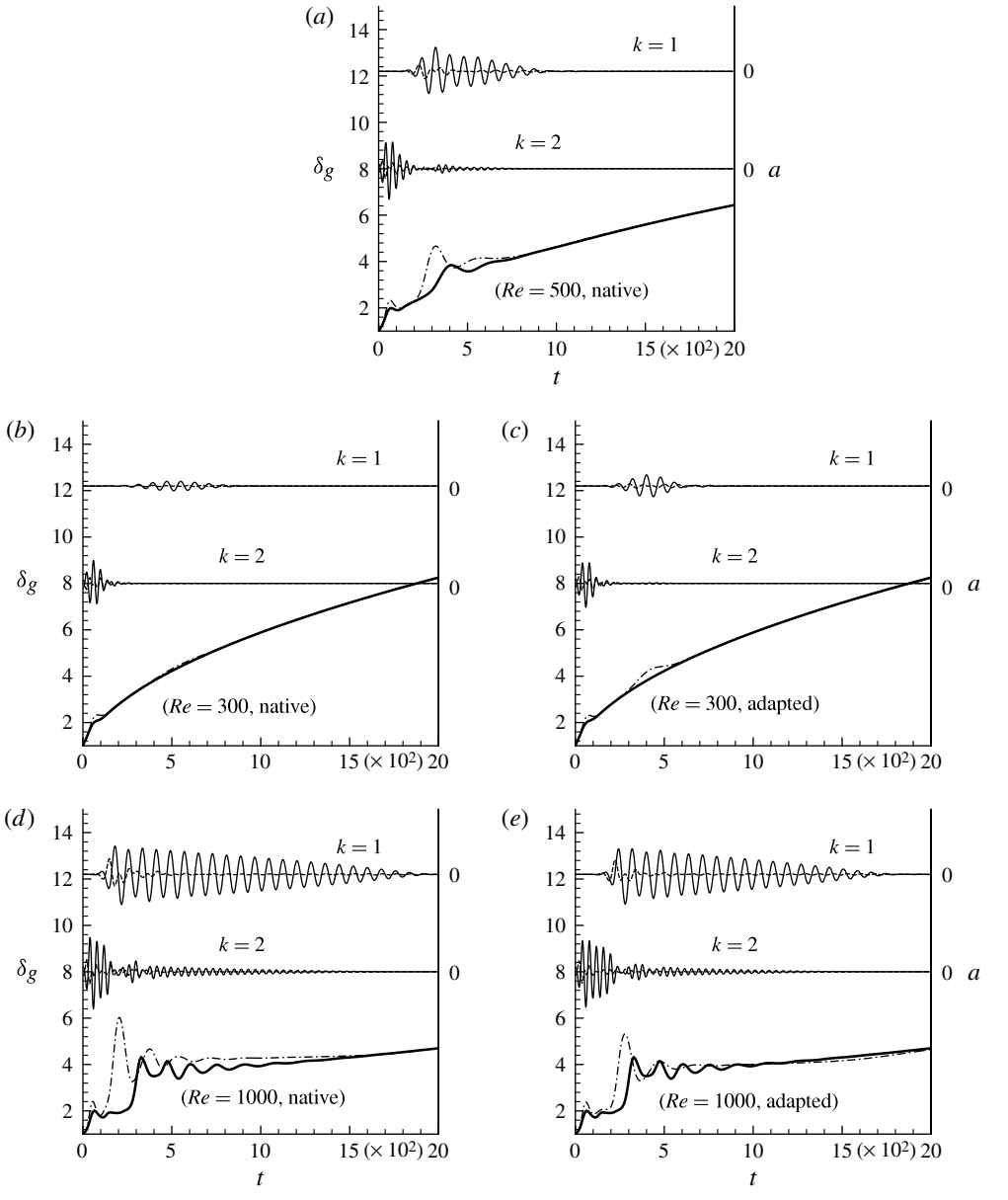


FIGURE 13. Comparison of native models and adapted models for the extension of Reynolds number from $Re = 500$ to $Re = 300$ and 1000. Here: ——, time coefficients $a_{11}(t)$ and $a_{21}(t)$; – – ––, time coefficients $a_{12}(t)$ and $a_{22}(t)$; and – · – · –, the shear layer thickness δ_g (for comparison, ——— is marked for the thickness computed from direct numerical simulation data at corresponding Reynolds numbers). The same scale is used for coefficients a in the comparison.

a compressible TD shear layer with its thickness varying in time, we introduced a scaling variable and its own dynamic equation to scale the space and applied POD-Galerkin projection on the scaled space for a much more efficient model in terms of the number of base modes. The modified POD-Galerkin projection results in models

https://doi.org/10.1017/jfm.2013.318 Published online by Cambridge University Press

at very low dimension with only a couple of Fourier-POD modes required in the description of compressible TD shear layers. The efficiency of the models is also marked by the energy efficiency of POD modes in the scaled space. The first POD modes of both spatial wavenumbers at $k = 1$ and $k = 2$ capture most of the energy while the second POD modes remain dynamically important despite their small energy contributions.

To capture basic dynamics, the compressible low-dimensional model requires only two POD modes for each wavenumber. Hence, a two-mode model is constructed by the projection of equations onto the first two POD modes of wavenumber $k = 1$. The two-mode model is able to capture single-wavenumber dynamics such as vortex roll-up. Similarly, a four-mode model is constructed by the projection of equations onto the first two POD modes of wavenumbers $k = 1$ and $k = 2$. The four-mode model is then able to capture the nonlinear interactions involving a fundamental wavenumber and its subharmonic, such as vortex pairing and merging.

Moreover, in comparison with the previous incompressible model by Wei & Rowley (2009), the compressible model provides a simpler mathematical model that guarantees the mass conservation without the need for a special coefficient matrix or special mapping (as used in the incompressible case). The compressible model uses the same inner product to define both POD modes and Galerkin projection, thus, the orthogonality is preserved in the process and leads to simple equations at the end. The compressible model includes the equation for thermodynamics, while the thermo-energy is also included in the energy-based norm. Although the compressible model does not increase the accuracy of the specific problem, it stands out by two obvious advantages: (i) simpler model equations (as a result of consistent orthogonality and simple scaling); and (ii) the inclusion of compressibility and thermodynamics.

Finally, as a step towards a more practical level, the model has been extended to apply to new Mach numbers and Reynolds numbers different from its original simulation parameters without additional numerical simulations. The adapted model shows robustness in both extensions and the model results match well with the benchmark simulations. In particular, we compared the results from adapted models, native models and the direct numerical simulations at different Mach numbers 0.2, 0.3 and 0.4 (for the same Reynolds number 500) and at different Reynolds numbers 300, 500 and 1000 (for the same Mach number 0.2). The adapted models provide results as good as those from native models and they are qualitatively correct in comparison with direct numerical simulations.

Acknowledgements

This work was partially supported by the Army Research Laboratory through the Army High Performance Computing Research Center (AHPCRC) and Micro Autonomous System & Technology (MAST) CTA. We thank H. Gao for his help in the revision. We also want to thank the referees for their thoughtful and constructive comments.

Appendix A. Isentropic Navier–Stokes equations

Here, we review the derivation of isentropic Navier–Stokes equations from compressible Navier–Stokes equations in full formulation (Zank & Matthaeus 1991; Batchelor 2000), which are

$$\frac{\mathrm{D}\rho}{\mathrm{D}t} + \rho\nabla \cdot \boldsymbol{u} = 0 \tag{A 1}$$

https://doi.org/10.1017/jfm.2013.318 Published online by Cambridge University Press

$$\rho \frac{\mathrm{D}\boldsymbol{u}}{\mathrm{D}t} = -\boldsymbol{\nabla} p + \boldsymbol{\nabla} \cdot \mathbb{T} \tag{A 2}$$

$$T \frac{\mathrm{D}s}{\mathrm{D}t} = \rho c_p \frac{\mathrm{D}T}{\mathrm{D}t} - \beta_T T \frac{\mathrm{D}p}{\mathrm{D}t} = \boldsymbol{\Phi} + k \nabla^2 T, \tag{A 3}$$

where

$$\mathbb{T} = 2\mu (e_{ij} - \tfrac{1}{3} \delta_{ij} \boldsymbol{\nabla} \cdot \boldsymbol{u}) \tag{A 4}$$

is the deviatoric stress tensor,

$$e_{ij} = \frac{1}{2} \left(\frac{\partial u_i}{\partial x_j} + \frac{\partial u_j}{\partial x_i} \right) \tag{A 5}$$

is the rate of strain tensor,

$$\beta_T = -\frac{1}{\rho} \left(\frac{\partial \rho}{\partial T} \right)_p \tag{A 6}$$

is the thermal expansion coefficient,

$$\boldsymbol{\Phi} = 2\mu (e_{ij} e_{ij} - \tfrac{1}{3} (\boldsymbol{\nabla} \cdot \boldsymbol{u})^2) \tag{A 7}$$

is the viscous dissipation, s is the entropy, T is the temperature, c_p is the specific heat under constant pressure and k is the thermal conductivity of the fluid.

For isentropic flow, we assume that $\mathrm{D}s/\mathrm{D}t = 0$, which is equivalent to neglecting the viscous dissipation $\boldsymbol{\Phi}$ and the heat conduction $k\nabla^2 T$. The energy equation reduces to

$$\rho c_p \frac{\mathrm{D}T}{\mathrm{D}t} = \beta_T T \frac{\mathrm{D}p}{\mathrm{D}t}. \tag{A 8}$$

Recall the equation of state $p = R\rho T$, where $R = c_p - c_v$ is the gas constant, c_v is the specific heat under constant volume. From the definition of β_T, one can get $\beta_T T = 1$. Substitute p from the equation of state, then the energy equation becomes

$$\rho \frac{\mathrm{D}T}{\mathrm{D}t} = \frac{(c_p - c_v)}{c_p} \frac{\mathrm{D}}{\mathrm{D}t} (\rho T). \tag{A 9}$$

Using the ratio of specific heat $\gamma = c_p/c_v$ instead, we have

$$\rho \frac{\mathrm{D}T}{\mathrm{D}t} = \frac{(\gamma - 1)}{\gamma} \left[\rho \frac{\mathrm{D}T}{\mathrm{D}t} + T \frac{\mathrm{D}\rho}{\mathrm{D}t} \right]. \tag{A 10}$$

Substitute $\mathrm{D}\rho/\mathrm{D}t$ and rearrange the equation to obtain

$$\frac{\mathrm{D}T}{\mathrm{D}t} + (\gamma - 1) T (\boldsymbol{\nabla} \cdot \boldsymbol{u}) = 0. \tag{A 11}$$

Substitute T from the equation of state to obtain

$$\frac{1}{\rho} \frac{\mathrm{D}p}{\mathrm{D}t} - \frac{p}{\rho^2} \frac{\mathrm{D}p}{\mathrm{D}t} + \frac{\gamma p}{\rho} (\boldsymbol{\nabla} \cdot \boldsymbol{u}) - \frac{p}{\rho} (\boldsymbol{\nabla} \cdot \boldsymbol{u}) = 0, \tag{A 12}$$

and then

$$\frac{1}{\rho} \frac{\mathrm{D}p}{\mathrm{D}t} + \frac{\gamma p}{\rho} (\boldsymbol{\nabla} \cdot \boldsymbol{u}) = 0, \tag{A 13}$$

https://doi.org/10.1017/jfm.2013.318 Published online by Cambridge University Press

with the continuity equation applied. Recall the first law of thermodynamics and Gibbs free energy equation $\mathrm{d}h = T\,rmds + \mathrm{d}p/\rho$, where h is the enthalpy, and $\mathrm{d}s = 0$ for isentropic flow. Applying the equation of state again

$$\frac{\gamma p}{\rho} = \gamma RT = c_p(\gamma - 1)T \tag{A 14}$$

and $c_pT = h$ for constant pressure process, the energy equation becomes

$$\frac{\mathrm{D}h}{\mathrm{D}t} + (\gamma - 1)h(\boldsymbol{\nabla} \cdot \boldsymbol{u}) = 0. \tag{A 15}$$

Introducing the speed of sound 'a' by $a^2 = \gamma p/\rho = (\gamma - 1)h$, we have

$$2a\frac{\mathrm{D}a}{\mathrm{D}t} = (\gamma - 1)\frac{\mathrm{D}h}{\mathrm{D}t}. \tag{A 16}$$

The energy equation is then described by a as

$$\frac{\mathrm{D}a}{\mathrm{D}t} + \frac{(\gamma - 1)}{2}a(\boldsymbol{\nabla} \cdot \boldsymbol{u}) = 0. \tag{A 17}$$

The relations between enthalpy, pressure and the speed of sound imply

$$\boldsymbol{\nabla} p = \rho \boldsymbol{\nabla} h = \frac{2\rho a}{\gamma - 1}\boldsymbol{\nabla} a. \tag{A 18}$$

So, the momentum equation becomes

$$\frac{\mathrm{D}\boldsymbol{u}}{\mathrm{D}t} = -\frac{2a}{\gamma - 1}\boldsymbol{\nabla} a + \nu\nabla^2\boldsymbol{u}, \tag{A 19}$$

where $\nu = \mu/\rho$. Finally, the isentropic Navier–Stokes equations are

$$\frac{\mathrm{D}\boldsymbol{u}}{\mathrm{D}t} + \frac{2a}{\gamma - 1}\boldsymbol{\nabla} a = \nu\nabla^2\boldsymbol{u} \tag{A 20}$$

$$\frac{\mathrm{D}a}{\mathrm{D}t} + \frac{(\gamma - 1)}{2}a\,(\boldsymbol{\nabla} \cdot \boldsymbol{u}) = 0. \tag{A 21}$$

We should keep in mind that the continuity equation is implied and already satisfied.

Appendix B. Equations and the coefficients in the two-mode model

The dynamic equations for the scaling variable g and coefficient vector $\boldsymbol{a} = (a_{1,1}a_{1,2})^{\mathrm{T}}$ for the two-mode model of temporal shear layer flow are

$$\dot{g} = \sum_{l,m=1}^{2} \frac{r_{lm}}{n_0}a_{1,m}a_{1,l}^{*}g + \frac{1}{Re}\frac{d_0}{n_0}g^3, \tag{B 1}$$

and

$$\dot{\boldsymbol{a}} = \left(\boldsymbol{B} + \frac{1}{Re}\boldsymbol{D} + \frac{\dot{g}}{g}\boldsymbol{E}\right)\boldsymbol{a}, \tag{B 2}$$

where matrices $\boldsymbol{B}$, $\boldsymbol{D}$ and $\boldsymbol{E}$ are defined by

$$\boldsymbol{B} = \begin{bmatrix} b_{11} + gc_{11} & b_{12} + gc_{12} \\ b_{21} + gc_{21} & b_{22} + gc_{22} \end{bmatrix}, \tag{B 3}$$

https://doi.org/10.1017/jfm.2013.318 Published online by Cambridge University Press

$$\boldsymbol{D} = \begin{bmatrix} -(2\pi/L)^2(n_{11}) + g^2 d_{11} & -(2\pi/L)^2(n_{12}) + g^2 d_{12} \\ -(2\pi/L)^2(n_{21}) + g^2 d_{21} & -(2\pi/L)^2(n_{22}) + g^2 d_{22} \end{bmatrix}, \tag{B 4}$$

$$\boldsymbol{E} = \begin{bmatrix} e_{11} & e_{12} \\ e_{21} & e_{22} \end{bmatrix}, \tag{B 5}$$

with all coefficients defined by

$$n_0 = \int \left(y \frac{\mathrm{d}u_0}{\mathrm{d}y} \right)^2 \mathrm{d}y, \quad d_0 = \int \frac{\mathrm{d}^2 u_0}{\mathrm{d}y^2} y \frac{\mathrm{d}u_0}{\mathrm{d}y} \, \mathrm{d}y, \tag{B 6a}$$

$$r_{lm} = -\int \left(\hat{v}_{1,m} \frac{\mathrm{d}\hat{u}^*_{1,l}}{\mathrm{d}y} + \hat{v}^*_{1,m} \frac{\mathrm{d}\hat{u}_{1,l}}{\mathrm{d}y} \right) y \frac{\mathrm{d}u_0}{\mathrm{d}y} \, \mathrm{d}y, \quad l, m = 1, 2. \tag{B 6b}$$

$$b_{lm} = -\frac{2\pi}{L} i \int \left(u_0 \hat{u}_{1,m} \hat{u}^*_{1,l} + u_0 \hat{v}_{1,m} \hat{v}^*_{1,l} + \beta u_0 \hat{a}_{1,m} \hat{a}^*_{1,l} + \beta\gamma a_0 \hat{a}_{1,m} \hat{u}^*_{1,l} + \frac{1}{\gamma} a_0 \hat{u}_{1,m} \hat{a}^*_{1,l} \right) \mathrm{d}y, \quad l, m = 1, 2. \tag{B 6c}$$

$$c_{lm} = -\int \left(\hat{v}_{1,m} \frac{\mathrm{d}u_0}{\mathrm{d}y} \hat{u}^*_{1,l} + \beta\gamma a_0 \frac{\mathrm{d}\hat{a}_{1,m}}{\mathrm{d}y} \hat{v}^*_{1,l} + \frac{1}{\gamma} a_0 \frac{\mathrm{d}\hat{v}_{1,m}}{\mathrm{d}y} \hat{a}^*_{1,l} \right) \mathrm{d}y, \quad l, m = 1, 2. \tag{B 6d}$$

$$n_{lm} = \int (\hat{u}_{1,m} \hat{u}^*_{1,l} + \hat{v}_{1,m} \hat{v}^*_{1,l}) \, \mathrm{d}y, \quad l, m = 1, 2. \tag{B 6e}$$

$$d_{lm} = \int \left(\frac{\mathrm{d}^2 \hat{u}_{1,m}}{\mathrm{d}y^2} \hat{u}^*_{1,l} + \frac{\mathrm{d}^2 \hat{v}_{1,m}}{\mathrm{d}y^2} \hat{v}^*_{1,l} \right) \mathrm{d}y, \quad l, m = 1, 2. \tag{B 6f}$$

$$e_{lm} = -\int \left(\frac{\mathrm{d}\hat{u}_{1,m}}{\mathrm{d}y} \hat{u}^*_{1,l} + \frac{\mathrm{d}\hat{v}_{1,m}}{\mathrm{d}y} \hat{v}^*_{1,l} + \beta \frac{\mathrm{d}\hat{a}_{1,m}}{\mathrm{d}y} \hat{a}^*_{1,l} \right) y \, \mathrm{d}y, \quad l, m = 1, 2. \tag{B 6g}$$

Appendix C. Equations and the coefficients in the four-mode model

For the four-mode model, the dynamic equations for the scaling variable g and coefficient vector $\boldsymbol{a} = (a_{1,1} a_{1,2} a_{2,1} a_{2,2})^{\mathrm{T}}$ are

$$\dot{g} = \sum_{l,m=1}^{2} \left(\frac{r_{1,lm}}{n_0} a_{1,m} a^*_{1,l} g + \frac{r_{2,lm}}{n_0} a_{2,m} a^*_{2,l} g \right) + \frac{1}{Re} \frac{d_0}{n_0} g^3, \tag{C 1}$$

and

$$\dot{\boldsymbol{a}} = \left(\boldsymbol{B} + \frac{1}{Re} \boldsymbol{D} + \frac{\dot{g}}{g} \boldsymbol{E} \right) \boldsymbol{a} + \boldsymbol{N}. \tag{C 2}$$

Matrices $\boldsymbol{B}$, $\boldsymbol{D}$ and $\boldsymbol{E}$ are linear terms of $a_{k,n}$ and have blocks of zeros as

$$\boldsymbol{B} = \begin{bmatrix} \boldsymbol{B}_1 & 0 \\ 0 & \boldsymbol{B}_2 \end{bmatrix}, \quad \boldsymbol{D} = \begin{bmatrix} \boldsymbol{D}_1 & 0 \\ 0 & \boldsymbol{D}_2 \end{bmatrix}, \quad \boldsymbol{E} = \begin{bmatrix} \boldsymbol{E}_1 & 0 \\ 0 & \boldsymbol{E}_2 \end{bmatrix}, \tag{C 3}$$

with submatrices defined by

$$\boldsymbol{B}_1 = \begin{bmatrix} b_{1,11} + g c_{1,11} & b_{1,12} + g c_{1,12} \\ b_{1,21} + g c_{1,21} & b_{1,22} + g c_{1,22} \end{bmatrix}, \quad \boldsymbol{B}_2 = \begin{bmatrix} b_{2,11} + g c_{2,11} & b_{2,12} + g c_{2,12} \\ b_{2,21} + g c_{2,21} & b_{2,22} + g c_{2,22} \end{bmatrix}, \tag{C 4a}$$

$$\boldsymbol{D}_1 = \begin{bmatrix} -(2\pi/L)^2 n_{1,11} + g^2 d_{1,11} & -(2\pi/L)^2 n_{1,12} + g^2 d_{1,12} \\ -(2\pi/L)^2 n_{1,21} + g^2 d_{1,21} & -(2\pi/L)^2 n_{1,22} + g^2 d_{1,22} \end{bmatrix}, \tag{C 4b}$$

https://doi.org/10.1017/jfm.2013.318 Published online by Cambridge University Press

$$\boldsymbol{D}_2 = \begin{bmatrix} -(4\pi/L)^2 n_{2,11} + g^2 d_{2,11} & -(4\pi/L)^2 n_{2,12} + g^2 d_{2,12} \\ -(4\pi/L)^2 n_{2,21} + g^2 d_{2,21} & -(4\pi/L)^2 n_{2,22} + g^2 d_{2,22} \end{bmatrix}, \tag{C 4c}$$

$$\boldsymbol{E}_1 = \begin{bmatrix} e_{1,11} & e_{1,12} \\ e_{1,21} & e_{1,22} \end{bmatrix}, \quad \boldsymbol{E}_2 = \begin{bmatrix} e_{2,11} & e_{2,12} \\ e_{2,21} & e_{2,22} \end{bmatrix}. \tag{C 4d}$$

The vector $\boldsymbol{N}$ includes all nonlinear terms of $a_{k,n}$ as

$$\boldsymbol{N} = \begin{bmatrix} N_{1,1} a_{1,1}^* a_{2,1} + N_{1,2} a_{1,1}^* a_{2,2} + N_{1,3} a_{1,2}^* a_{2,1} + N_{1,4} a_{1,2}^* a_{2,2} \\ N_{2,1} a_{1,1}^* a_{2,1} + N_{2,2} a_{1,1}^* a_{2,2} + N_{2,3} a_{1,2}^* a_{2,1} + N_{2,4} a_{1,2}^* a_{2,2} \\ N_{3,1} a_{1,1} a_{1,1} + N_{3,2} a_{1,1} a_{1,2} + N_{3,3} a_{1,2} a_{1,1} + N_{3,4} a_{1,2} a_{1,2} \\ N_{4,1} a_{1,1} a_{1,1} + N_{4,2} a_{1,1} a_{1,2} + N_{4,3} a_{1,2} a_{1,1} + N_{4,4} a_{1,2} a_{1,2} \end{bmatrix}, \tag{C 5}$$

where nonlinear coefficients are defined as

$$\begin{aligned} N_{1,1} &= b_{1,111} + g c_{1,111}, & N_{2,1} &= b_{1,211} + g c_{1,211}, \\ N_{1,2} &= b_{1,112} + g c_{1,112}, & N_{2,2} &= b_{1,212} + g c_{1,212}, \\ N_{1,3} &= b_{1,121} + g c_{1,121}, & N_{2,3} &= b_{1,221} + g c_{1,221}, \\ N_{1,4} &= b_{1,122} + g c_{1,122}, & N_{2,4} &= b_{1,222} + g c_{1,222}, \end{aligned} \tag{C 6a}$$

$$\begin{aligned} N_{3,1} &= b_{2,111} + g c_{2,111}, & N_{4,1} &= b_{2,211} + g c_{2,211}, \\ N_{3,2} &= b_{2,112} + g c_{2,112}, & N_{4,2} &= b_{2,212} + g c_{2,212}, \\ N_{3,3} &= b_{2,121} + g c_{2,121}, & N_{4,3} &= b_{1,221} + g c_{2,221}, \\ N_{3,4} &= b_{2,122} + g c_{2,122}, & N_{4,4} &= b_{2,222} + g c_{2,222}. \end{aligned} \tag{C 6b}$$

The coefficients are each defined in indicial notation as

$$n_0 = \int \left(y \frac{\mathrm{d}u_0}{\mathrm{d}y} \right)^2 \mathrm{d}y, \quad d_0 = \int \frac{\mathrm{d}^2 u_0}{\mathrm{d}y^2} y \frac{\mathrm{d}u_0}{\mathrm{d}y}\, \mathrm{d}y, \tag{C 7a}$$

$$r_{1,lm} = -\int \left(\hat{v}_{1,m} \frac{\mathrm{d}\hat{u}_{1,l}^*}{\mathrm{d}y} + \hat{v}_{1,m}^* \frac{\mathrm{d}\hat{u}_{1,l}}{\mathrm{d}y} \right) y \frac{\mathrm{d}u_0}{\mathrm{d}y} \mathrm{d}y, \quad l, m = 1, 2. \tag{C 7b}$$

$$r_{2,lm} = -\int \left(\hat{v}_{2,m} \frac{\mathrm{d}\hat{u}_{2,l}^*}{\mathrm{d}y} + \hat{v}_{2,m}^* \frac{\mathrm{d}\hat{u}_{2,l}}{\mathrm{d}y} \right) y \frac{\mathrm{d}u_0}{\mathrm{d}y} \mathrm{d}y, \quad l, m = 1, 2. \tag{C 7c}$$

$$\begin{aligned} b_{1,lm} = -\frac{2\pi}{L} \mathrm{i} \int \Big(& u_0 \hat{u}_{1,m} \hat{u}_{1,l}^* + u_0 \hat{v}_{1,m} \hat{v}_{1,l}^* + \beta u_0 \hat{a}_{1,m} \hat{a}_{1,l}^* \\ & + \beta\gamma a_0 \hat{a}_{1,m} \hat{u}_{1,l}^* + \frac{1}{\gamma} a_0 \hat{u}_{1,m} \hat{a}_{1,l}^* \Big) \mathrm{d}y, \quad l, m = 1, 2. \end{aligned} \tag{C 7d}$$

$$\begin{aligned} b_{2,lm} = -\frac{4\pi}{L} \mathrm{i} \int \Big(& u_0 \hat{u}_{2,m} \hat{u}_{2,l}^* + u_0 \hat{v}_{2,m} \hat{v}_{2,l}^* + \beta u_0 \hat{a}_{2,m} \hat{a}_{2,l}^* \\ & + \beta\gamma a_0 \hat{a}_{2,m} \hat{u}_{2,l}^* + \frac{1}{\gamma} a_0 \hat{u}_{2,m} \hat{a}_{2,l}^* \Big) \mathrm{d}y, \quad l, m = 1, 2. \end{aligned} \tag{C 7e}$$

$$c_{1,lm} = -\int \left(\hat{v}_{1,m} \frac{\mathrm{d}u_0}{\mathrm{d}y} \hat{u}_{1,l}^* + \beta\gamma a_0 \frac{\mathrm{d}\hat{a}_{1,m}}{\mathrm{d}y} \hat{v}_{1,l}^* + \frac{1}{\gamma} a_0 \frac{\mathrm{d}\hat{v}_{1,m}}{\mathrm{d}y} \hat{a}_{1,l}^* \right) \mathrm{d}y, \quad l, m = 1, 2. \tag{C 7f}$$

$$c_{2,lm} = -\int \left(\hat{v}_{2,m} \frac{\mathrm{d}u_0}{\mathrm{d}y} \hat{u}_{2,l}^* + \beta\gamma a_0 \frac{\mathrm{d}\hat{a}_{2,m}}{\mathrm{d}y} \hat{v}_{2,l}^* + \frac{1}{\gamma} a_0 \frac{\mathrm{d}\hat{v}_{2,m}}{\mathrm{d}y} \hat{a}_{2,l}^* \right) \mathrm{d}y, \quad l, m = 1, 2. \tag{C 7g}$$

$$n_{1,lm} = \int (\hat{u}_{1,m} \hat{u}_{1,l}^* + \hat{v}_{1,m} \hat{v}_{1,l}^*) \mathrm{d}y, \quad l, m = 1, 2. \tag{C 7h}$$

https://doi.org/10.1017/jfm.2013.318 Published online by Cambridge University Press

$$n_{2,lm} = \int (\hat{u}_{2,m}\hat{u}^*_{2,l} + \hat{v}_{2,m}\hat{v}^*_{2,l})\mathrm{d}y, \quad l, m = 1, 2. \tag{C 7i}$$

$$d_{1,lm} = \int \left(\frac{\mathrm{d}^2\hat{u}_{1,m}}{\mathrm{d}y^2}\hat{u}^*_{1,l} + \frac{\mathrm{d}^2\hat{v}_{1,m}}{\mathrm{d}y^2}\hat{v}^*_{1,l} \right) \mathrm{d}y, \quad l, m = 1, 2. \tag{C 7j}$$

$$d_{2,lm} = \int \left(\frac{\mathrm{d}^2\hat{u}_{2,m}}{\mathrm{d}y^2}\hat{u}^*_{2,l} + \frac{\mathrm{d}^2\hat{v}_{2,m}}{\mathrm{d}y^2}\hat{v}^*_{2,l} \right) \mathrm{d}y, \quad l, m = 1, 2. \tag{C 7k}$$

$$e_{1,lm} = -\int \left(y\frac{\mathrm{d}\hat{u}_{1,m}}{\mathrm{d}y}\hat{u}^*_{1,l} + y\frac{\mathrm{d}\hat{v}_{1,m}}{\mathrm{d}y}\hat{v}^*_{1,l} + \beta y\frac{\mathrm{d}\hat{a}_{1,m}}{\mathrm{d}y}\hat{a}^*_{1,l} \right) \mathrm{d}y, \quad l, m = 1, 2. \tag{C 7l}$$

$$e_{2,lm} = -\int \left(y\frac{\mathrm{d}\hat{u}_{2,m}}{\mathrm{d}y}\hat{u}^*_{2,l} + y\frac{\mathrm{d}\hat{v}_{2,m}}{\mathrm{d}y}\hat{v}^*_{2,l} + \beta y\frac{\mathrm{d}\hat{a}_{2,m}}{\mathrm{d}y}\hat{a}^*_{2,l} \right) \mathrm{d}y, \quad l, m = 1, 2. \tag{C 7m}$$

$$b_{1,lmj} = -\frac{4\pi}{L}i \int \left(\hat{u}^*_{1,m}\hat{u}_{2,j}\hat{u}^*_{1,l} + \hat{u}^*_{1,m}\hat{v}_{2,j}\hat{v}^*_{1,l} + \beta\hat{u}^*_{1,m}\hat{a}_{2,j}\hat{a}^*_{1,l} + \beta\gamma\hat{u}^*_{1,m}\hat{a}_{2,j}\hat{u}^*_{1,l} + \frac{1}{\gamma}\hat{u}^*_{1,m}\hat{u}_{2,j}\hat{a}^*_{1,l} \right) \mathrm{d}y, \quad l, m, j = 1, 2. \tag{C 7n}$$

$$b_{2,lmj} = -\frac{2\pi}{L}\mathrm{i} \int \left(\hat{u}_{1,m}\hat{u}_{1,j}\hat{u}^*_{2,l} + \hat{u}_{1,m}\hat{v}_{1,j}\hat{v}^*_{2,l} + \beta\hat{u}_{1,m}\hat{a}_{1,j}\hat{a}^*_{2,l} + \beta\gamma\hat{u}_{1,m}\hat{a}_{1,j}\hat{u}^*_{2,l} + \frac{1}{\gamma}\hat{u}_{1,m}\hat{u}_{1,j}\hat{a}^*_{2,l} \right) \mathrm{d}y, \quad l, m, j = 1, 2. \tag{C 7o}$$

$$c_{1,lmj} = -\int \left(\hat{v}^*_{1,m}\frac{\mathrm{d}\hat{u}_{2,j}}{\mathrm{d}y}\hat{u}^*_{1,l} + \hat{v}_{2,m}\frac{\mathrm{d}\hat{u}^*_{1,j}}{\mathrm{d}y}\hat{u}^*_{1,l} + \hat{v}^*_{1,m}\frac{\mathrm{d}\hat{v}_{2,j}}{\mathrm{d}y}\hat{v}^*_{1,l} + \hat{v}_{2,m}\frac{\mathrm{d}\hat{u}^*_{1,j}}{\mathrm{d}y}\hat{v}^*_{1,l} + \beta\gamma a^*_{1,m}\frac{\mathrm{d}\hat{a}_{2,j}}{\mathrm{d}y}\hat{v}^*_{1,l} + \beta\gamma a_{2,m}\frac{\mathrm{d}\hat{a}^*_{1,j}}{\mathrm{d}y}\hat{v}^*_{1,l} + \beta v^*_{1,m}\frac{\mathrm{d}\hat{a}_{2,j}}{\mathrm{d}y}\hat{a}^*_{1,l} + \beta v^*_{2,m}\frac{\mathrm{d}\hat{a}^*_{1,j}}{\mathrm{d}y}\hat{a}^*_{1,l} + \frac{1}{\gamma}a^*_{1,m}\frac{\mathrm{d}\hat{v}_{2,j}}{\mathrm{d}y}\hat{a}^*_{1,l} + \frac{1}{\gamma}a_{2,m}\frac{\mathrm{d}\hat{v}^*_{1,j}}{\mathrm{d}y}\hat{a}^*_{1,l} \right) \mathrm{d}y, \quad l, m, j = 1, 2. \tag{C 7p}$$

$$c_{2,lmj} = -\int \left(\hat{v}_{1,m}\frac{\mathrm{d}\hat{u}_{1,j}}{\mathrm{d}y}\hat{u}^*_{2,l} + \hat{v}_{1,m}\frac{\mathrm{d}\hat{v}_{1,j}}{\mathrm{d}y}\hat{v}^*_{2,l} + \beta\gamma a_{1,m}\frac{\mathrm{d}\hat{a}_{1,j}}{\mathrm{d}y}\hat{v}^*_{2,l} + \beta v_{1,m}\frac{\mathrm{d}\hat{a}_{1,j}}{\mathrm{d}y}\hat{a}^*_{2,l} + \frac{1}{\gamma}a_{1,m}\frac{\mathrm{d}\hat{v}_{1,j}}{\mathrm{d}y}\hat{a}^*_{2,l} \right) \mathrm{d}y, \quad l, m, j = 1, 2. \tag{C 7q}$$

REFERENCES

AMSALLEM, D. & FARHAT, C. 2008 Interpolation method for adapting reduced-order models and application to aeroelasticity. *AIAA J.* **46** (7), 1803–1813.

AREF, H. 1983 Integrable, chaotic, and turbulent vortex motion in two-dimensional flows. *Annu. Rev. Fluid Mech.* **15** (1), 345–389.

AREF, H. & SIGGIA, E. D. 1980 Vortex dynamics of the two-dimensional turbulent shear layer. *J. Fluid Mech.* **100** (04), 705–737.

BATCHELOR, G. 2000 *An Introduction to Fluid Dynamics*. Cambridge University Press.

BOGDANOFF, D. W. 1983 Compressiblity effects in turbulent shear layers. *AIAA J.* **21**, 926–927.

BRADSHAW, P. 1977 Compressible turbulent shear layers. *Annu. Rev. Fluid Mech.* **9**, 33–54.

BROWN, G. L. & ROSHKO, A. 1974 On density effects and large structure in turbulent mixing layers. *J. Fluid Mech.* **64**, 775–816.

CHOMAZ, J.-M. 2005 Global instabilities in spatially developing flows: non-normality and nonlinearity. *Annu. Rev. Fluid Mech.* **37**, 357–392.

COLONIUS, T., LELE, S. K. & MOIN, P. 1993 Boundary conditions for direct computation of aerodynamic sound generation. *AIAA J.* **31**, 1574–1582.

https://doi.org/10.1017/jfm.2013.318 Published online by Cambridge University Press

COLONIUS, T., LELE, S. K. & MOIN, P. 1997 Sound generation in a mixing layer. *J. Fluid Mech.* **330**, 375–409.

DAY, M. J., MANSOUR, N. N. & REYNOLDS, W. C. 2001 Nonlinear stability and structure of compressible reacting mixing layers. *J. Fluid Mech.* **446**, 375–408.

DEANE, G. E., KEVREKIDIS, I. G., KARNIADAKIS, G. E. & ORSZAG, S. A. 1991 Low-dimensional models for complex geometry flows: application to grooved channels and circular cylinders. *Phys. Fluids* A **3**, 2337–2354.

DRAZIN, P. G. & REID, W. H. 2004 *Hydrodynamic Stability*, 2nd edn. Cambridge University Press.

ELLIOTT, G. S., SAMIMY, M. & ARNETTE, S. A. 1995 The characteristics and evolution of large-scale structures in compressible mixing layers. *Phys. Fluids* **7** (4), 864–876.

FREUND, J. B. 1997 Proposed inflow/outflow boundary condition for direct computation of aerodynamic sound. *AIAA J.* **35** (4), 740–742.

HO, C. M. & HUERRE, P. 1984 Perturbed free shear layers. *Annu. Rev. Fluid Mech.* **16**, 365–424.

HOLMES, P., LUMLEY, J. L. & BERKOOZ, G. 1996 *Turbulence, Coherent Structures, Dynamical Systems and Symmetry*. Cambridge University Press.

LIEU, T. & FARHAT, C. 2007 Adaptation of aeroelastic reduced-order models and application to an F-16 configuration. *AIAA J.* **45** (6), 1244–1257.

LIEU, T. & LESOINNE, M. 2004 Parameter adaptation of reduced order models for three-dimensional flutter analysis. *AIAA Paper* 2004-0888.

LOCK, R. C. 1951 The velocity distribution in the laminar boundary layer between parallel streams. *Q. J. Mech. Appl. Maths* **4** (1), 42–63.

LUCHTENBURG, D. M., GÜNTER, B., NOACK, B. R., KING, R. & TADMOR, G. 2009 A generalized mean-field model of the natural and actuated flows around a high-lift configuration. *J. Fluid Mech.* **623**, 283–316.

MONKEWITZ, P. A. & HUERRE, P. 1982 Influence of the velocity ratio on the spatial instabilty of mixing layers. *Phys. Fluids* **25**, 1137–1143.

MOSER, R. D. & ROGERS, M. M. 1993 The three-dimensional evolution of a plane mixing layer: pairings and transition to turbulence. *J. Fluid Mech.* **247**, 275–320.

NOACK, B., AFANASIEV, K., MORZYŃSKI, M., TADMOR, G. & THIELE, F. 2003 A hierarchy of low-dimensional models for the transient and post-transient cylinder wake. *J. Fluid Mech.* **497**, 335–363.

NOACK, B. R. & ECKELMANN, H. 1994 A global stability analysis of the steady and periodic cylinder wake. *J. Fluid Mech.* **270**, 297–330.

PAPAMOSCHOU, D. & ROSHKO, A. 1988 The compressible turbulent shear layer: an experimental study. *J. Fluid Mech.* **197**, 453–477.

POTTER, O. E. 1957 Laminar boundary layers at the interface of co-current parallel streams. *Q. J. Mech. Appl. Maths* **10** (3), 302–311.

ROGERS, M. M. & MOSER, R. D. 1992 The three-dimensional evolution of a plane mixing layer: the Kelvin–Holmholtz rollup. *J. Fluid Mech.* **243**, 183–226.

ROWLEY, C. W., COLONIUS, T. & MURRAY, R. M. 2004 Model reduction for compressible flow using POD and Galerkin projection. *Physica* D **189** (1–2), 115–129.

ROWLEY, C. W., KEVREKIDIS, I. G., MARSDEN, J. E. & LUST, K. 2003 Reduction and reconstruction for self-similar dynamical systems. *Nonlinearity* **16**, 1257–1275.

ROWLEY, C. W. & MARSDEN, J. E. 2000 Reconstruction equations and the Karhunen–Loève expansion for systems with symmetry. *Physica* D **142**, 1–19.

SAFFMAN, P. G. & BAKER, G. R. 1979 Vortex interactions. *Annu. Rev. Fluid Mech.* **11**, 95–122.

SANDHAM, N. D. 1994 The effect of compressibility on vortex pairing. *Phys. Fluids* **6** (2), 1063–1072.

SANDHAM, N. D. & REYNOLDS, W. C. 1990 Compressible mixing layer: linear theory and direct simulation. *AIAA J.* **28**, 618–624.

SCHLICHTING, H. & GERSTEN, K. 2000 *Boundary-Layer Theory*, 8th edn. Springer.

SCHMID, P. J. & HENNINGSON, D. S. 2001 *Stability and Transition in Shear Flows*, Applied Mathematical Sciences, vol. 142. Springer.

https://doi.org/10.1017/jfm.2013.318 Published online by Cambridge University Press

SCHMIDT, R. & GLAUSER, M. 2004 Improvements in low dimensional tools for flow-structure interaction problems: using global POD. *AIAA Paper* 2004-0889.

TADMOR, G., LEHMANN, O., NOACK, B. R. & MORZYNSKI, M. 2010 Mean field representation of the natural and actuated cylinder wake. *Phys. Fluids* **22**, 034102.

THUROW, B., SAMIMY, M. & LEMPERT, W. 2003 Compressibility effects on turbulence structures of axisymmetric mixing layers. *Phys. Fluids* **15** (6), 1755–1765.

URBAN, W. D. & MUNGAL, M. G. 2001 Planar velocity measurements in compressible mixing layers. *J. Fluid Mech.* **431**, 189–222.

WEI, M. & FREUND, J. B. 2006 A noise-controlled free shear flow. *J. Fluid Mech.* **546**, 123–152.

WEI, M., QAWASMEH, B. R., BARONE, M., VAN BLOEMEN WAANDERS, B. G. & ZHOU, L. 2012 Low-dimensional model of spatial shear layers. *Phys. Fluids* **24** (1), 014108.

WEI, M. & ROWLEY, C. W. 2009 Low-dimensional models of a temporally evolving free shear layer. *J. Fluid Mech.* **618**, 113–134.

WINANT, C. D. & BROWAND, F. K. 1974 Vortex pairing: the mechanism of turbulent mixing-layer growth at moderate Reynolds number. *J. Fluid Mech.* **63** (02), 237–255.

ZANK, G. P. & MATTHAEUS, W. H. 1991 The equations of nearly incompressible fluids. I. Hydrodynamics, turbulence, and waves. *Phys. Fluids* A **3** (1), 69–82.

https://doi.org/10.1017/jfm.2013.318 Published online by Cambridge University Press